

# A Dexterous and Compliant (DexCo) Hand Based on Soft Hydraulic Actuation for Human Inspired Fine In-hand Manipulation

Jianshu Zhou *Member, IEEE*, Junda Huang, Qi Dou, Pieter Abeel, *Fellow, IEEE*, and Yunhui Liu, *Fellow, IEEE*

**Abstract**—Human beings possess a remarkable skill for fine in-hand manipulation, utilizing both intra-finger interactions (in-finger) and finger-environment interactions across a wide range of daily tasks. These tasks range from skilled activities like screwing light bulbs, picking and sorting pills, and in-hand rotation, to more complex tasks such as opening plastic bags, cluttered bin picking, and counting cards. Despite its prevalence in human activities, replicating these fine motor skills in robotics remains a substantial challenge. This study tackles the challenge of fine in-hand manipulation by introducing the dexterous and compliant (DexCo) hand system. The DexCo hand mimics human dexterity, replicating the intricate interaction between the thumb, index, and middle fingers, with a contractable palm. The key to maneuverable fine in-hand manipulation lies in its innovative soft hydraulic actuation, which strikes a balance between control complexity, dexterity, compliance, and motion accuracy within a compact structure, enhancing the overall performance of the system. The model of soft hydraulic actuation, based on hydrostatic force analysis, reveals the compliance of hand joints, which is also further extended to a dedicated ROS package for DexCo hand simulation, considering both motion and stiffness aspects. Dedicated velocity and position teleoperation controllers are designed for implementing real physical manipulation tasks. The benchmark results show that the fingertip achieves a maximum repeatable finger strength of 34.4 N, a grasp cycle time of less than 2.04 s, and a maximum repeatability accuracy of 0.03 mm. Experimental results demonstrate the DexCo hand successfully performs complex fine in-hand manipulation tasks, providing a promising solution for advancing robotic manipulation capabilities toward the human level.

**Index Terms**—Robotic Hand, Grasping and Manipulation, Soft Robotics, Soft Actuation, Proprioception.

## I. INTRODUCTION

Robotic manipulation systems have emerged as promising solutions to address labor shortages, reduce costs, and collaborate in daily living tasks. Despite numerous advancements in robotic grasping, a persistent gap remains between

human and robotic performance in dexterous manipulation [1]. Humans possess an inherent skill for fine in-hand manipulation (Fig. 1A), utilizing dexterous interactions both intra-finger (in-finger) and between fingers and environment (finger-environment) for various daily tasks. Replicating these fine in-hand manipulation skills in robotics remains a formidable challenge [2], necessitating innovative approaches to bridge existing disparities from robot design, sensing, and control perspectives.

Over the past decades, research has focused on two main directions in robotic hand development. One direction involves anthropomorphic robotic hands with high dexterity and general functionality, which come with high complexity [3], [4]. The other direction focuses on the simpler grippers with straightforward designs tailored for specific and desired tasks. In recent years, dexterous anthropomorphic hands have become available for a wider range of manipulation tasks, thanks to advancements in compliant mechanisms [5]–[8] and learning-based algorithms [9]–[11]. These improvements simplify the uncertainties of complex physical interactions during manipulation. However, previous efforts have demonstrated that achieving a delicate balance between control complexity, compliance, dexterity, motion accuracy, and system complexity remains both desirable and challenging.

To address the intricate balance required for robotic in-hand manipulation, this study introduces the DexCo hand system utilizing soft hydraulic actuation. It covers hand design, actuation, modeling, and control strategies (Fig. 1B). Rigorous experiments were carried out to characterize the system and offer design customization recommendations. The results demonstrate that our DexCo hand successfully achieves fine in-hand manipulation tasks, showcasing its potential as a solution for robotic dexterous in-hand manipulation towards the human level (Fig. 1C). The contribution of this work is summarized in five parts:

- Propose DexCo Hand with anthropomorphic design consideration, integrating flexion, adduction/abduction, finger opposition, and palm dexterity for human-like in-hand manipulability (Fig. 3A). Benchmark experiments indicate that the grasp strength ranges from 20.14 N to 38.24 N (Tab. IV) and cycle times ranging from 1.02 s to 2.04 s (Tab. V).
- Propose the soft hydraulic actuation approach, crucial for controllable in-hand manipulation. This approach effectively balances robotic hand control complexity, dexterity, compliance, and accuracy, providing a comprehensive

This project is supported in part by the Shenzhen Portion of Shenzhen-Hong Kong Science and Technology Innovation Cooperation Zone under HZQB-KCZYB-20200089, in part by the InnoHK Clusters of the Hong Kong SAR Government via the Hong Kong Centre for Logistics Robotics, and in part by the Research Grants Council of Hong Kong (GRF 14207423). Corresponding to Qi Dou and Yunhui Liu.

Jianshu Zhou, Junda Huang, and Yunhui Liu are with Department of Mechanical and Automation Engineering, The Chinese University of Hong Kong. (jianshuzhou@cuhk.edu.hk; jianshuzhou@berkeley.edu; jdhuang99@link.cuhk.edu.hk; yhlui@cuhk.edu.hk)

Qi Dou is with the Department of Computer Science and Engineering, The Chinese University of Hong Kong. (qdou@cse.cuhk.edu.hk)

Pieter Abeel holds concurrent appointments as a Professor at UC Berkeley and as an Amazon Scholar. This paper describes work performed at UC Berkeley and is not associated with Amazon. (pabeel@berkeley.edu)

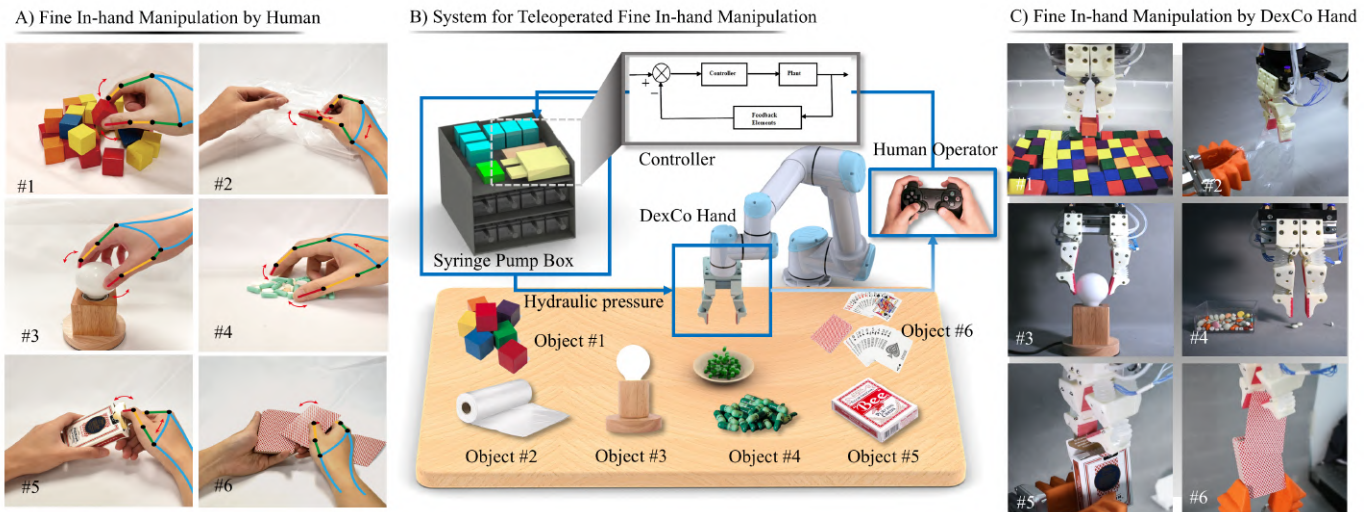


Fig. 1. (A) Typical fine in-hand manipulation tasks performed by human. (#1) cluttered bin picking; (#2) opening a sealed plastic bag; (#3) screwing on and off light bulb; (#4) picking and sorting granular objects; (#5) Opening card box and extracting cards from card box; (#6) counting cards. (B) The teleoperated robotic system to perform various grasping and manipulation tasks. (C) Human inspired fine in-hand manipulation tasks realized by the proposed DexCo Hand.

solution.

- Extend DexCo hand dexterity and compliance models to a hand simulator. The model, incorporating hydrostatic force analysis, effectively illustrates hand joint motion and compliance. A dedicated ROS package has been developed to simulate the DexCo hand, showcasing its capabilities and development in a virtual environment.
- Design dedicated velocity and position teleoperation controllers for executing real-world physical manipulation tasks effectively.
- Propose a twist strength benchmark and comprehensive hand evaluation, including fundamental assessments and real manipulation tasks, to enhance robotic fine in-hand manipulation towards human-comparable dexterity and performance levels.

The paper begins with a thorough review of related works on dexterous hands and manipulation in Section II, emphasizing our unique contributions. Section III elaborates on the innovative structure and design of the dexterous hand, utilizing soft hydraulic actuation with dedicated modeling. In Section IV, the paper develops models to quantify manipulability and compliance of the hand, provides a tool to evaluate and enhance the design efficiently. Dedicated fundamental experimental characterizations are presented in Section V, followed by Section VI, which demonstrates the hand's fine in-hand manipulation capabilities. The conclusion and future work are then discussed. The appendix provides details on calibration, simulator development, and controller design.

## II. RELATED WORKS

This section is dedicated to reviewing related work in three key aspects of in-hand manipulation: design, actuation, and sensing. By summarizing existing approaches, we aim to highlight the differences and innovations of our approach in addressing current challenges.

### A. Hand Design

The structural configurations of robotic hands encompass various elements such as the number of fingers, degrees of freedom (DoF) of the fingers, finger layout, topological structure of links, joint types, and structural materials. These variations, further cooperating with sensing, control, and interaction, impact the complexity of the robotic hand. Despite its simplicity, the two-finger parallel gripper remains widely used, featuring two single-segment fingers with a single degree of freedom. Movement is achieved through a linear guide rail or a rotary linkage mechanism. Another variant employs rotational joints for object envelopment and securing, with optimizations in topological structure by Rodríguez et al. [12], [13]. Soft robotics has introduced a soft material counterpart of the two-finger gripper [14], with attempts to enhance variable stiffness using rigid substances [15]–[17]. Overall, two-finger grippers excel in single tasks like pinch grasping [18] and power grasping [19]–[21], performing manipulation such as pushing [22]–[24], and extrinsic dexterity [25]–[27] utilizing environment.

Increasing the number of fingers and joints enhances task diversity [28]–[30] and performs well in specific tasks [31], such as sliding, rotation, pushing, extrinsic dexterity, and caging. Mason proposed a stable multi-fingered hand with single rotational degrees of freedom per finger [31]. Multi-jointed two-fingered hands strike a balance between complexity, reliability, and task diversity, such as the Velo gripper [32], which uses revolute joints with a pulley system to adaptively grasp objects with pinch-power switching capability. Other designs, such as Yoon et al.'s linkage mechanism [33] and Kim et al.'s belt and linkage structures [34], offer adaptability to different grasping surfaces and switchable grasping modes. Roller joints introduced by Yuan et al. [35], [36] achieve dexterity surpassing that of the human hand in specific tasks. The Model W hand by Bircher et al. [37] introduces translational freedom to the palm, enhancing manipulation through caging.

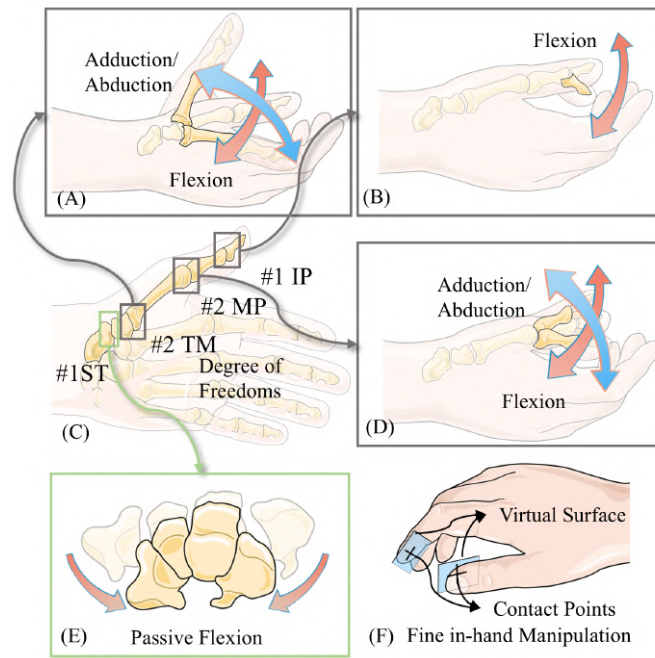


Fig. 2. (A) Two active dofs at trapezo-metacarpal (TM) joint. (B) One active dof at interphalangeal (IP) joint. (C) The degree of freedoms for human thumb. (D) Two active dofs at metacarpophalangeal (MP) joint. (E) One passive dof at the metacarpals joint. This dof initiates the flexion motion of thumb. (F) Virtual contact surface and contact points when human perform in-finger manipulation.

On the other hand, the soft counterparts, such as the SDM hand [38] and its derivatives [39]–[47] by Dollar et al. feature compliance from soft structures at joints, enhancing robustness in unstructured environments. The authors previously proposed that the pneumatic soft-rigid hybrid hand offers improved grasping adaptiveness and robustness [48]. By incorporating lateral degrees of freedom [49], this solution also demonstrates early lateral manipulation capabilities and lateral compliance. Furthermore, [50] demonstrates an extension of pneumatic joints integrated with a tendon-driven approach. While gas-tendon coupled actuation offers tendon-driven control and gas-driven compliance, it faces limitations: redundant system design, challenging tendon layout, synchronization issues, interference, and reduced control precision over time. These challenges, including accuracy, compliance, control complexity, and quantifiable modeling, continue to affect pneumatic soft-rigid hybrid joints, limiting their utilization in more complex manipulation tasks.

Early anthropomorphic hands, such as the Salisbury hand [51], modular hand [52], Pisa/IIT hand [53], [54], and others [55]–[57], were designed to perform general manipulation. While recent learning methods, including reinforcement learning and imitation learning, have improved task diversity and robustness, challenges related to actuation, structure, control complexity, and hardware portability persist. These issues hinder the ability to obtain training data, define tasks, and bridge the sim-to-real gap, limiting algorithmic capabilities and exploration of task diversity. Soft multi-segment hands [58], [59] and soft anthropomorphic hands, such as the RBO

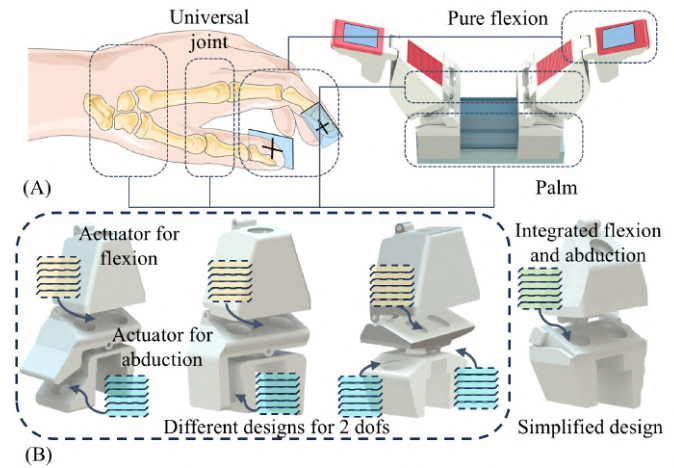


Fig. 3. Mapping from human hand to robotics hand. (A) The corresponding relationship between each part of the human hand and the robotic hand. (B) Different mechanical realization of adduction/abduction freedom.

Hand [21], [52], tactile hand [60], and BCL-26 [8], enhance environmental adaptability and reduce control complexity. However, current designs still face challenges, such as complex control, difficulty obtaining effective training data, lack of simulation capabilities, reliance on hardcoded movements, and limited dexterity and precision. As a result, compliant hands remain effective for adaptive grasping but struggle to demonstrate clear advantages in more complex manipulation tasks, like fine manipulation, where balancing control complexity, dexterity, compliance, and accuracy is still a challenge.

## B. Hand Actuation

Robotic hand actuation methods are primarily motor-driven or fluid-driven. Motor-driven methods include gears, linkages, slides, or cable drives [34], [35], [37], [61]. Cable-driven actuation, popular in dexterous hands [32], [38], [51], [54], [62], offers a more compact structure, enabling higher degrees of freedom, but introducing control complexity [63]. Fluid-driven actuation [64], including hydraulics and pneumatics, gains popularity in soft robotics [65], offering functional, compact, and lightweight grippers [66]–[68].

Actuation complexity can be classified as fully-actuated or underactuated systems. Fully-actuated systems have higher hardware and control complexity [69], [70], while underactuated systems simplify algorithms and control, facilitating diverse grasping and manipulation tasks [8], [28].

## C. Hand Sensing

The position and force sensing of a dexterous hand greatly influence the reliability of algorithm development for these devices. Many proprioception schemes for dexterous hands rely on external methods, such as using cameras [71]–[73] or motion capture systems [28], [74] to obtain the posture of the dexterous hand. Internal sensing methods, such as servos [9], encoders, and magnetic encoders, can provide high-precision angle feedback. However, due to installation location and size constraints, the applicability of these internal sensing solutions



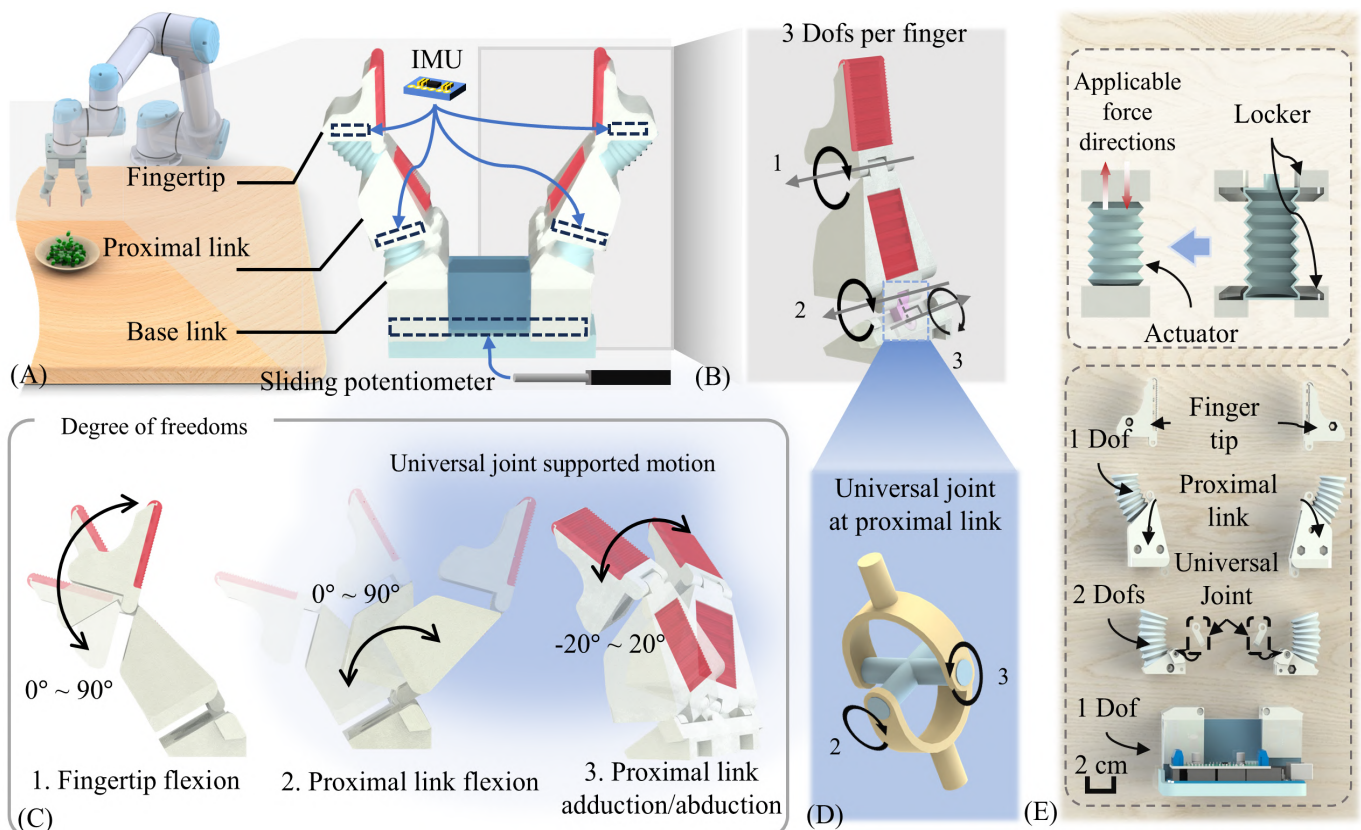


Fig. 4. (A) Front view of the DexCo Hand and the sensor installation positions. (B) Structure and three degrees of freedom (DoFs) of the finger. (C) Finger motions generated from the three DoFs. (D) Universal joint connecting the proximal link and base link. (E) The assembly method for actuators and an exploded view of the DexCo Hand.

is limited. For instance, they are not feasible for use with ball joints or flexible joints. Emerging sensing methods for soft robotics also offer new perspectives for dexterous hand proprioception. Aaron and others have used optical fiber to sense flexure at soft robotic joints [39], while Wang and Huang, among others, have utilized flexible inductive sensors to provide feedback on linear and rotational movements, as well as spatial posture [66], [75]. Wang and colleagues have employed custom magnetic fields to sense two degrees of rotational freedom [76]. However, the main issues with these novel methods are accuracy, hysteresis, and durability.

### III. DEXCO HAND DESIGN

This section introduces the design details of the DexCo hand, including anthropomorphic structure and kinematics, soft hydraulic actuation and modeling, and hand proprioception.

#### A. Structure and Kinematics

The dexterity and compliance of the human hand enable it to handle complex interactions and rich contacts[2], [77]. The thumb has six degrees of freedom (as shown in Fig. 2C). Starting from the fingertip, these are the interphalangeal (IP) joint (Fig. 2B), the metacarpophalangeal (MP) joint (Fig. 2D), the trapezo-metacarpal (TM) joint (Fig. 2A), and the scapho-trapezian (ST) joint (Fig. 2E). The ST joint is a passive degree

of freedom that provides an initial flexion movement when the thumb moves. The other five degrees of freedom are active. The dual degrees of freedom of the MP and TM joints arise from their saddle-shaped structure, which allows movements similar to a universal joint. For fine in-hand manipulation (including grasping), for which the human hand is particularly adept, the thumb and index finger need to have either direct or indirect contact, which can be abstracted into a 'contact point' and a 'virtual surface' (Fig. 2F). Thus, three degrees of freedom of the thumb are used to align the contact point, and the other two are used to align the virtual surface, as referenced in Kapandji [78]. Overall, these six degrees of freedom enable the thumb to flexibly adjust its orientation and position relative to the palm. Additionally, the index finger of the human hand has two flexion degrees of freedom near the fingertip and flexion, adduction/abduction degrees of freedom at the base.

The intuitive direction is to imitate the functionality of the human index finger and thumb, achieving fine in-hand manipulation. To this end, we abstracted and mimicked three characteristics from the manipulation process between the thumb and index finger and then applied them to the two-fingered hand, as shown in Fig. 3A. The first is the flexion motion, which is common in two-fingered hands. Flexion, whether in a single joint or multiple joints, provides the ability to grasp, as well as the capacity for manipulation skills like sliding, pushing, and caging. Another characteristic is the adduction/abduction movement of human fingers (Fig. 3B). This

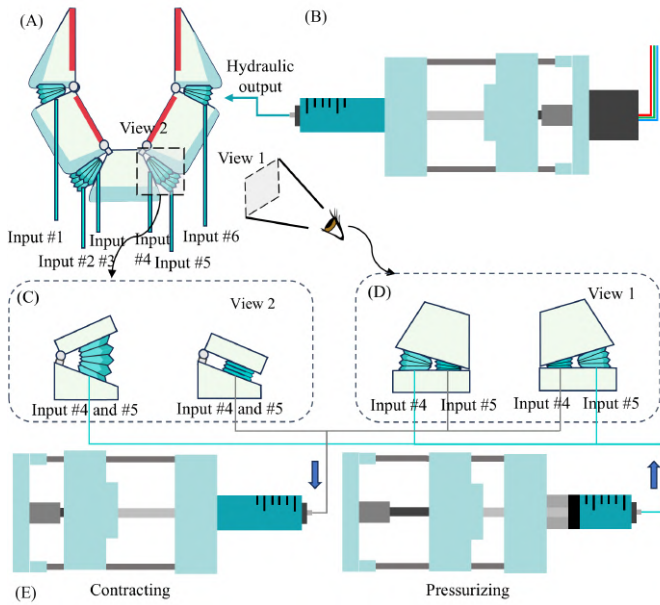


Fig. 5. Actuation mechanism. (A) Illustration of DexCo hand. (B) Hydraulic syringe pump. (C) The flexion motion from the front view. (D) The adduction/abduction motion from the side view. (E) Contracting and pressurizing mode for hydraulic syringe pump.

adduction/abduction movement is observable in all fingers. We noted that adduction/abduction movements are essential for performing certain tasks and can improve the efficiency and robustness of others. Without these movements, tasks may require wrist and arm movements, necessitating complex modeling and control. This indicates that adduction/abduction has the potential to significantly enhance the functionality and efficiency of robotic hands. The final feature is the large motion range of the thumb relative to the palm. This feature is derived from the high dexterity and suited skeleton length of the thumb. However, integrating all six degrees of freedom into a single finger, even if passive, would increase the complexity of actuation and proprioception, leading to reduced reliability, as noted in Quigley et al. [52]. Therefore, considering that two of the six degrees of freedom help the thumb adjust the virtual surface, the opposition structure of the two-fingered hand can eliminate the dependence on these two degrees of freedom. Further, we ensure each finger has three degrees of freedom (two for flexion, one for adduction/abduction) to align the contact point (Fig. 2F), which is fundamental for dexterity. Additionally, we use one degree of freedom in the palm to accommodate the thumb's ability to move across a wide range relative to the palm using multiple degrees of freedom.

The DexCo hand, as shown in Fig. 4A and 4E, features modular fingers. Each finger is composed of three links: the base, proximal, and fingertip link. These links encompass three degrees of freedom, formed by two joints as illustrated in Fig. 4B. The joints consist of a two-degree-of-freedom universal joint at the proximal end and a revolute joint at the fingertip. One rotational axis of the universal joint is parallel to the fingertip's rotational axis, enabling two independent degrees of freedom for flexion movements. The other degree of freedom of the universal joint, perpendicular to

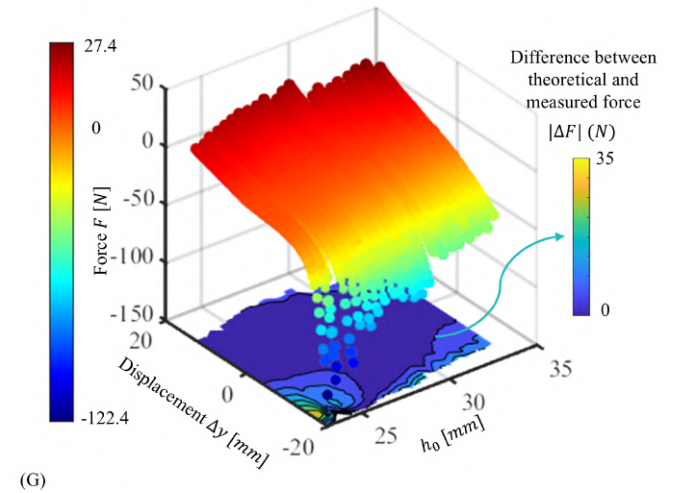
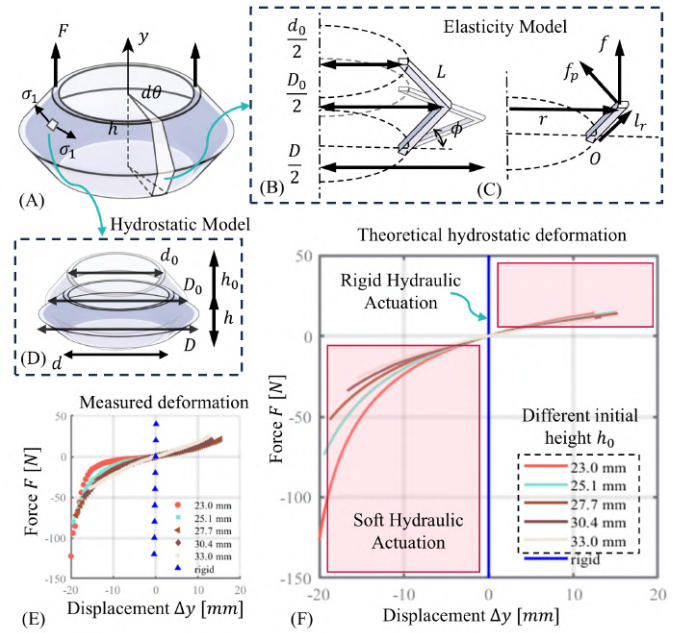


Fig. 6. (A) One convolution of the origami actuator. (B) and (C) are involved in the elastic force modeling. (B) shows a  $d\theta$  section of the actuator and the geometric constraints used in elastic force analysis. (C) shows an infinitesimal element of the section. (D) Hydrostatic modeling based on a thin wall piece and the geometric constraints applied in hydrostatic modeling. (E) The measured deformation model. (F) The theoretical deformation model with an emphasis on the comparison between soft and rigid hydraulic actuation. (H) Full illustration of measured deformation and the difference with the theoretical model. The bottom contour shows the difference between measured and theoretical force.

the flexion axis, facilitates adduction/abduction movements, as shown in Fig. 4C and 4D. The use of the universal joint significantly reduces the complexity of the fingers in performing adduction/abduction movements. Other designs, as shown in Fig. 3B, which continue to use traditional cascaded revolute joints, encounter several challenges. From a control perspective, multi-stage cascading introduces the maximum inertia at the proximal end, reducing control stability. In terms of kinematics, longer fingers generally decrease dexterity. From a sensing perspective, more actuators mean more sensors are needed, leading to a larger and more complex system. The range of motion for each joint is illustrated in Fig. 4C. The

fingertip rotational joint ranges from  $0^\circ$  to  $90^\circ$ . The universal joint's range of motion in the flexion direction extends from  $0^\circ$  to  $90^\circ$ , and in the adduction/abduction direction, it ranges from  $-20^\circ$  to  $20^\circ$ .

These two modular fingers are mounted on a pneumatic slide that performs linear motion, which we refer to as the palm (Fig. 4E). The palm (SMC MHF2-12D2R) is pneumatically driven and can withstand a range of air pressures, supporting a relatively large gripping force (48N). With two pneumatic inputs, the slide can control both stiffness and position. It has a travel distance of 60mm, which provides significant dexterity for fine in-hand operations during experimental tasks. Observations from experiments suggest that increasing the slide's travel distance could further enhance operational dexterity.

### B. Soft Hydraulic Actuation

The soft hydraulic actuation mechanism is a pivotal aspect of the proposed design, illustrated in Figures 5 and 6, seamlessly integrates dexterity and compliance into a compact form. The refined origami (Bellow type) actuators, showcased in Figures 5C 5E, exhibit excellent airtightness, durability, and a high expansion ratio, contributing to the effective driving of the revolute joint. The driving principles of the revolute joint have been extensively detailed in our previous work [66], ??.

Operating under hydrostatic pressure, this mechanism provides accuracy, local compliance, and bidirectional driving capabilities. The intrinsic properties of hydraulic actuation ensure accuracy and stability, while local compliance leverages the benefits of soft materials, creating a resilient interaction space and reducing the risk of hardware damage. Building on this mechanism, the integration of a universal joint closely replicates the dexterous base joint of a human finger (Fig. 5C and 5D) with the simplest actuation. The base joint is actuated by a pair of hydraulic actuators through differential actuation. This innovative approach empowers the mechanical hand to achieve universal joint motion with minimal complexity and facilitates the easy embedding of proprioception. Collectively, these features enable the mechanical hand to replicate the functions of human thumbs and index fingers while optimizing the hardware structure to the greatest extent possible.

The design of the origami actuators revolves around two key aspects: customization of the actuator's behavior through design parameters and consideration of specific materials and fabrication methods based on functional requirements. Design parameters, outlined in Table I, focus on modifying the zig-zag origami characteristics. Adjusting the relative angle between two adjacent zig-zag features, for example, allows for the alteration of the actuator's initial length. Similarly, modifying the depth-to-diameter ratio influences the mechanical characteristics of the actuator during motion, while changing the number of origami layers directly impacts its expansion length.

In terms of fabrication, the actuator needs to meet the force output requirements of the dexterous hand, requiring a certain level of pressure resistance. Given the challenge of manufacturing small-scale, pressure-resistant, and airtight actuators, we selected blow molding as the preferred method.

Polyethylene, chosen for its toughness and extensibility, serves as the material for blow molding. This choice ensures that the actuators can maintain thinness without compromising durability, even after undergoing repeated positive and negative pressure cycles and extreme position movements.

The origami actuator is hydraulically driven, as depicted in Figure 5B. On one hand, in contrast to pneumatic actuators, which exhibit notable compressibility, hydraulic actuators offer higher stiffness during the interaction. For dexterous hand applications, lower stiffness is not always desirable, as it may require the introduction of a variable stiffness mechanism, thereby increasing system complexity and control challenges [49]. The higher stiffness of the hydraulic actuators ensures a proportional relationship between the volume of the liquid and the length of the actuator even under external forces. This characteristic facilitates the driving of the two degrees of freedom in the configuration space of the universal joint: simultaneous elongation or shortening of both actuators induces flexion, while differential elongation and shortening result in adduction/abduction movements of the universal joint.

TABLE I  
MAJOR PARAMETERS AND VARIABLES OF THE  
SS-ACTUATORS

Parameters	Values
Inner diameter: $d_0$ ( mm)	14
Initial outer diameter: $D_0$ ( mm)	22
Chamber wall thickness: $t$ ( mm)	0.2
Number of convolutions: $N$	6
Young's modulus (MPa)	87
Poisson's ratio	0.38
Inner diameter (mm)	$d$
Outer diameter (mm)	$D$
Chamber wall length (mm)	$l_r$
Initial height of one convolution (mm)	$h_0$
Height of one convolution (mm)	$h$
Initial volume of one convolution ( $\text{mm}^3$ )	$V_0$
Volume of one convolution ( $\text{mm}^3$ )	$V$
Pressure in soft actuator (MPa)	$P$

On the other hand, conventional rigid hydraulic actuation bears similarity to motor actuation, lacking inherent compliance and necessitating active force control for the interaction, as illustrated in Figure 6A. In contradistinction, soft hydraulic actuation integrates the advantageous features of a soft actuator and hydraulic actuation, concurrently achieving forceful output, inherent compliance, and optimal actuation efficiency, as depicted in Figure 6F. Here, we aim to obtain a deformation model for the hydraulic actuators, i.e.,

$$F \triangleq g(h_0, \Delta y) = F_e + F_h \quad (1)$$

where  $h_0$  represents the initial height of the actuators,  $F_e$  is the elastic force that is always used in pneumatic actuation modeling [66], [79],  $F_h$  represents the hydrostatic force. We tune the initial height by hydraulically pressurizing the actuators. This model describes the relationship between force

$F$  and linear deformation  $\Delta y$  under a certain initial height of the actuator. The main parameters and variables involved in the derivation are shown in Table I.

**Elastic Force Modeling** Wang et al. [79] demonstrated the elastic force of a hollow origami tube under external force, while our model further considered the actuator's internal pressure force. This internal pressure force becomes prominent when the actuation media changes from low density to high density.

Firstly, as the upper and lower halves of a single-convolution origami actuator are symmetrical (Fig. 6A), their strains are identical. Based on Castigliano's theorem, we can derive

$$\delta y = 2 \frac{\partial U}{\partial f} = 2 \int_{d/2}^{D/2} \frac{M}{EI} \frac{\partial M}{\partial f} dr \quad (2)$$

where  $U$  is the strain energy,  $f$  is the force on an infinitesimal element of the actuator (Fig. 6B), i.e.  $f = F_e \cdot \frac{d\theta}{2\pi}$ ,  $\delta y$  is the displacement of one convolution of the actuator,  $M$  is the torque at the current position  $r$ ,  $E$  is Young's modulus, and  $I$  is the moment of inertia at the current infinitesimal element, i.e.  $I = \frac{t^3}{12(1-\mu^2)} r d\theta$ .

The torque  $M$  and its partial derivative are

$$M = \underbrace{f \left( r - \frac{d}{2} \right)}_{M_f} + \underbrace{Pd\theta \left( \frac{1}{3} \cos \phi \cdot l_r^3 + \frac{d}{4} l_r^2 \right)}_{M_{fp}} \quad (3)$$

$$\frac{\partial M}{\partial f} = r - \frac{d}{2} + \frac{8}{d^2} \left( \frac{1}{3} \cos \phi \cdot l_r^3 + \frac{d}{4} l_r^2 \right) \quad (4)$$

where  $r$  is the distance from the actuator wall to the central axis,  $P$  is the internal pressure of the fluid,  $l_r = \frac{r-d/2}{\cos \phi}$ . In Eq. 3, the left side  $f \left( r - \frac{d}{2} \right)$ ,  $M_f$ , is the torque produced by force  $f$ , and the right side  $Pd\theta \left( \frac{1}{3} \cos \phi \cdot l_r^3 + \frac{d}{4} l_r^2 \right)$ ,  $M_{fp}$ , is the torque on the actuator's wall produced by internal pressure (Fig. 6C). The pressure torque is obtained through the integral of pressure force along the chamber length,  $\int_0^{lr} Pl \cdot y d\theta dl$ , where  $l$  is the distance from  $O$  along the actuator's wall. Substituting Eq. 3 and Eq. 4 into Eq. 2, we can derive the function  $F_e(h_0, \Delta y, D)$  by integrating the polynomial equation 2.

On the other hand, during actuator deformation, the geometric constraints between  $\Delta y$ ,  $D$ , and  $d$  are based on the constant liquid volume. However, for simplification, we make an assumption below for the geometric constrain:

**Assumption 1** The length of the actuator's wall  $L$  is constant, i.e.,  $L \triangleq \sqrt{\left( \frac{D_0-d_0}{2} \right)^2 + \left( \frac{h_0}{2} \right)^2}$ , and the inner diameter is assumed to be constant, i.e.,  $d \triangleq d_0$ .

Based on *assumption 1*, we derive:

$$D = d + \sqrt{h_0^2 + (D_0 - d)^2 - \left( \frac{\Delta y}{N} + h_0 \right)^2} \quad (5)$$

where  $d_0$  is assumed constant,  $h$  is the height of one convolution of the actuator, and  $D_0$  is the initial outer diameter. Combining Eq. 2 ~ 5, the elastic force model  $F_e(h_0, \Delta y)$  is attained, whose range is within  $-0.5 \sim 0.15$  N. The force

generated from the elastic force in these thinwalled soft actuators is rather small. Therefore, when effecting, hydrostatic force plays a vital role in interaction.

**Hydrostatic Force Modeling** The hydrostatic force is also generated from the elastic deformation of the soft actuator. However, the elastic force results from the elastic deformation in the axial direction due to the compression or extension of the soft actuator, which could be referred to as a spring (Fig. 6B). The hydrostatic force is generated from the elastic deformation on the radial direction in the compression or extension phase (Fig. 6D), which could be referred to as blowing a balloon. To attain the hydrostatic pressure, we make the geometric constrain

**Assumption 2** Under an initial height of the soft actuator  $h_0$ , the volume of water is constant during the motion phase, i.e.,  $V = V_0 \triangleq \text{constant}$ .

Based on the *assumption 2*, we have the geometric constrain

$$\begin{cases} V_0 = \frac{\pi h_0}{3} \left[ \left( \frac{D_0}{2} \right)^2 + \left( \frac{D_0}{2} \right)^2 + \frac{D_0 d_0}{4} \right] \\ V = \frac{\pi h}{3} \left[ \left( \frac{D}{2} \right)^2 + \left( \frac{D}{2} \right)^2 + \frac{Dd}{4} \right] \\ V = V_0 \end{cases} \quad (6)$$

where variables are shown in the Table. I. To derive the deformation in the radial direction, we compute the radial strain based on the thin-walled theory. Firstly, as shown in Figure 6A, stress  $\sigma_1$  is attained based on the axial profile

$$\sigma_1 = \frac{Pr}{t} \quad (7)$$

where  $r$  represents the radius at height  $y$ . Then, according to the generalized hooker's law

$$\varepsilon_1 = \frac{\sigma_1}{E} = \frac{\Delta_1}{2\pi r} \quad (8)$$

where  $\Delta_1$  is the difference of the circumference under the stress,  $\varepsilon_1$  represents the strain on the circumference. Therefore, based on Eq. 7 and Eq. 8, we attain the inner diameter and outer diameter under pressure  $P$ :

$$\begin{cases} d = d_0 + \frac{2P}{Et} \cdot \left( \frac{d_0}{2} \right)^2 \\ D = D_0 + \frac{2P}{Et} \cdot \left( \frac{D_0}{2} \right)^2 \end{cases} \quad (9)$$

where  $P \triangleq -\frac{4}{\pi d_0^2} F_h$ .

Incorporating Eq. 9 into Eq. 6, we obtain the solution, i.e.,  $F_h = F_h(h_0, \Delta y)$ , by solving a quadratic equation. As  $F_h \gg F_e$ , we have  $F \approx F_h$ . These results are presented in Figure 6(E ~ H), illustrating the effectiveness of soft hydraulic actuation, which relies on the hydrostatic force within soft materials. Compared to soft actuation, rigid hydraulic actuation, as shown in Figure 6F, has a significantly higher theoretical stiffness, a claim supported by the measured forces depicted in Figure 6E. The capabilities of soft hydraulic actuation are showcased in Figure 6F, demonstrating its ability to achieve on-demand compliance while providing adequate force output. Figure 6H offers a comprehensive view of the measured forces, highlighting the force discrepancies between actual measurements and theoretical predictions at the bottom contour of the graph. Most areas within this contour display



slight differences, affirming the accuracy of the hydrostatic analysis. However, a notable deviation occurs at the corners, attributed to unforeseen radial deformations.

**Actuation** Finally, the actuation of the hand is divided into two integral components: origami actuators seamlessly integrated into the hand and a syringe pump system situated at the back end, as illustrated in Figures 5A and 5B. Each origami actuator is equipped with a syringe pump as its driver. The syringe pump comprises a syringe, a stepper motor, a motor driver, and a magnetic encoder. The syringe is directly linked to the origami actuator, propelling its movement. When the volume inside the syringe is compressed, the origami actuator elongates; conversely, as the volume increases, the origami actuator shortens. This actuation method, referred to as direct pumping in [80], allows the syringe to utilize volumes ranging from 10 ml to 250 ml, precisely matching the volume of the origami actuator. To achieve high-speed actuation and substantial output force, a 57 stepper motor is chosen as the driver for the syringe pumps. The 57 stepper motor can efficiently drive a 250 ml syringe at high speeds. The synchronization of multiple stepper motors is accomplished through the IIC bus in conjunction with a microcontroller. This approach has successfully achieved low-latency synchronous movement within eight stepper motors, meeting the stringent requirements for synchronized control of multiple degrees of freedom essential for the dexterous hand in this study. Additionally, magnetic encoders provide high-precision feedback on the position of the stepper motors, facilitating closed-loop control of the syringe pumps.

### C. DexCo Hand Proprioception

The proprioception system of the DexCo hand is primarily dedicated to sensing joint angles, which predominantly incorporates two types of sensors: a linear sliding potentiometer and an Inertial Measurement Unit (IMU). The linear potentiometer is positioned at the palm joint, providing accurate feedback on the distance of the hand's opening and closing. On the other hand, the IMU is fixed to the proximal and fingertip links of the fingers, offering feedback on the revolute joints. Commercially available IMUs often consist of various MEMS (Micro-Electro-Mechanical Systems) integrated chips, encompassing a 3-axis accelerometer, a 3-axis gyroscope, a 3-axis magnetometer, and other measurement units such as barometers and thermometers for compensating drifts like temperature drift. This integration facilitates the convenient incorporation of the IMU into small spaces, such as within a finger, while still providing multi-axis rotational information.

The DexCo hand employs a commercially available MEMS IMU (ICM-20948, TDK InvenSense), a 9-axis IMU integrating accelerometers, gyroscopes, and magnetometers. To obtain the angle of the fingertip, the difference between the readings from the fingertip IMU and the proximal IMU is directly calculated. As the roll and pitch angles exhibit minimal drift, we align the x-axis of both IMUs parallel to the rotational axis of the fingertip not only reduces computational demands but also ensures minimal drift.

For acquiring the dual-axis angles of the universal joint, calculations are based on the known palm posture and Euler

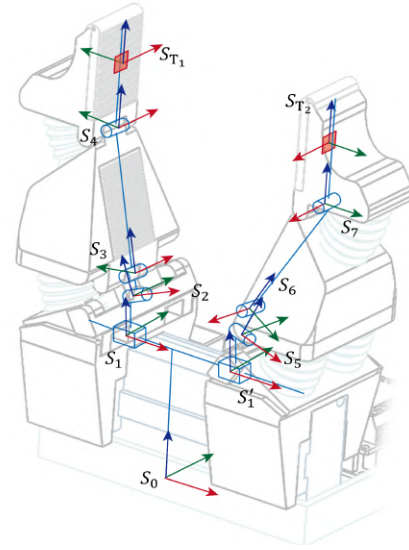


Fig. 7. Kinematic structure of the DexCo hand.

angles from the proximal IMU. Taking one finger as an example, the configuration space includes  $q_2, q_3$ , and  $q_4$  (As shown in the Fig. 7, configuration space is corresponding to each frame  $S_i$ ). The angle of the fingertip,  $q_4$ , can be obtained by taking the difference between the corresponding angles from two IMUs, while the universal joint angles  $q_2$  and  $q_3$  are derived from the rotations in the configuration space as below.

$$\begin{cases} R_y\left(-\frac{\pi}{6}\right) R_x(q_2) R_z\left(\frac{\pi}{2}\right) R_x(q_3) = {}^0R_3 \\ R_y\left(\frac{\pi}{6}\right) R_x(q_5) R_z\left(-\frac{\pi}{2}\right) R_x(q_6) = {}^0R_6 \end{cases} \quad (10)$$

Since the base of the hand is fixed to the end of the robotic arm, the posture of the palm base is known. By utilizing the IMU on the proximal link and the posture of the palm, we can obtain the rotation matrix  ${}^0R_2$  of the proximal link relative to the base. The  $R_x(q_2) R_z\left(\frac{\pi}{2}\right) R_x(q_3)$  in Eq. 10 represents the rotation matrix for the XZX Euler angles. Thus, we can determine the angles of the universal joint through the Eq. 10. Unfortunately, the IMU can only provide stable feedback for angular data. Positional data, derived through the integration of accelerometer readings, suffers from significant drift issues. If not for this limitation, it would have been possible to determine the width of the palm using the two proximal IMUs.

## IV. DEXCO HAND MODELING

This section explores DexCo hand modeling, emphasizing manipulability and compliance as crucial metrics for quantitatively evaluating hand manipulation performance, reflecting the two key distinctive performance indices of the DexCo hand.

**1) Dexterity and Manipulability Modeling:** The section discusses the dexterity of the DexCo hand from two kinematic perspectives: the manipulability of a single finger and the manipulability of the entire hand. The manipulability of a single finger primarily considers two aspects. First, from the perspective of symmetry. Since the three degrees of freedom (DoF) of the two fingers are symmetrical, the forces acting



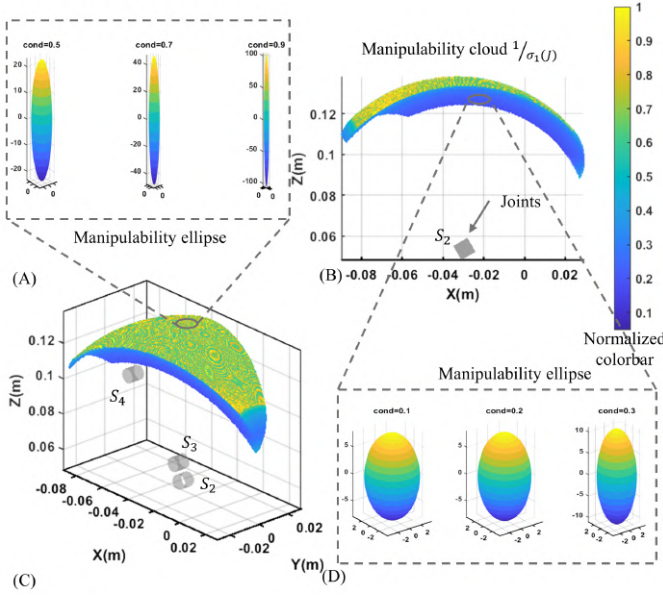


Fig. 8. Manipulability analysis and compliance analysis of a single finger. (A) Manipulability ellipse at the upper boundary of the cartesian working space. (B) The view of manipulability cloud from the xz-plane. The color bar is applied to (B), (C), (E) and (G). (C) Manipulability cloud of a single finger. The upper boundary has a larger singularity, therefore has a lower manipulability. (D) Manipulability ellipse below the upper boundary of the cartesian working space. As a lower value means higher manipulability, the blue area has a better manipulability under the singularity metric. (E) Compliance cloud in cartesian space. The value at each point is attained based on the volume metric. (F) Compliance ellipse at the extremum. (G) Compliance cloud in cartesian space. The value at each point is attained based on the condition number metric. Take the logarithm of the condition number, and then normalize the result.

on the object (vector field) [62] or the manipulability in space can be regarded as the superposition of two identical fields. Second, from the principle of minimization. If the DexCo hand is viewed as comprising one three-DoFs finger and one four-DoFs finger (including the palm dof), the manipulability of the configuration is determined by the finger with lesser dofs, i.e.,  $\sigma(\chi) = \min(\sigma(\chi_1), \sigma(\chi_2))$ . On the other hand, the manipulability of the entire hand considers all seven degrees of freedom, where  $S_{T1}$  is set as the reference frame, and  $S_{T2}$  as the operating frame (Fig. 7).

Considering the manipulability of a single finger. As previously mentioned, the homogeneous transformation matrix for the single finger with three degrees of freedom is represented as:

$${}^0T_{T1} = {}^0T_1 {}^1T_2 {}^2T_3 {}^3T_4 {}^4T_{T1} := \begin{bmatrix} {}^0R_{T1} & {}^0p_{T1} \\ 0 & 1 \end{bmatrix} \quad (11)$$

where  ${}^0R_{T1} \in \mathbb{R}^{3 \times 3}$  denotes the rotation matrix from the frame  $S_0$  to the end-effector frame  $S_{T1}$ , and  ${}^0p_{T1} \in \mathbb{R}^3$  represents the translation from  $S_0$  to  $S_{T1}$ . We focus on translational manipulability in this analysis. Meanwhile, we fix  $q_1$  as constant in matrix  ${}^0T_{T1}$ , which indicates no movement in the palm. Consequently, the configuration space is defined as  $q = [q_2, q_3, q_4]^T \in \mathbb{R}^3$ . The Jacobian matrix is,

$$J(q) = \frac{\partial p}{\partial q} \in \mathbb{R}^{3 \times 3} \quad (12)$$

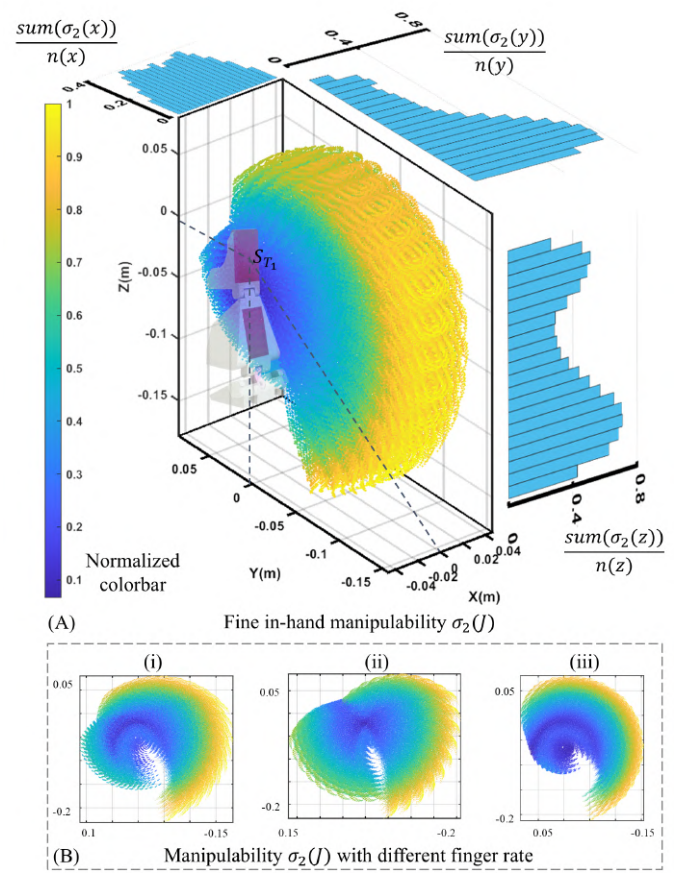


Fig. 9. Manipulability analysis of the whole hand. (A) The reference frame is selected as  $S_{T1}$ . The operating frame is selected as  $S_{T2}$ . The 3D view shows in-finger manipulability without considering obstacles. Other plots show the distribution of the average manipulability on three axis. (B) YZplane view of different finger linkage lengths: (i) length ratio alike a human finger (1:1), (ii) longer length on the middle link (ratio 1:5), (iii) longer length on the fingertip link (ratio 5:1).

Excluding  $q_1$  in the analysis of manipulability serves two purposes. On one hand, it eliminates the translational redundancy in cartesian space, thus simplifying the Jacobian matrix analysis. On the other hand,  $q_1$  doesn't affect the manipulability metric  $\sigma_1$ : the redundancy of  $q_1$  is equivalent to a translational superposition in the manipulability cloud of  $q$ , as shown in Figure 8C. Therefore, it is reasonable to analyze only the 3-DoFs for DexCo hand.

According to [81], [82], the manipulability of a single serial mechanism can be defined as the inverse condition number of the Jacobian matrix in the entire workspace,

$$\sigma_1(J) = \frac{1}{\text{cond}(J(q))} = \frac{s_{\min}}{s_{\max}} \quad (13)$$

or the product of the eigenvalues of the Jacobian matrix,

$$\sigma_2(J) = \sqrt{\det(J(q) \cdot J(q)^T)} = \sqrt{s_1 s_2 \dots s_n} \quad (14)$$

where  $s_i$  is the eigenvalue of the matrix  $(J \cdot J^T)$ ,  $s_{\min}$  and  $s_{\max}$  are the minimum and maximum eigenvalues. These two manipulability metrics measure different features.  $\sigma_1$  represents the ratio of the shortest to the longest axis of the manipulability ellipsoid (as detailed in appendix B). A smaller

TABLE II  
TRANSFORMATION OF STIFFNESS AND COMPLIANCE OF CONTACT INTERFACE

<b>stiffness</b>	$K_a = J_a^T K_q J_a$	$K_q = J_q^T K_f J_q$	$K_f = H^T K_{tr} H$	$H^T K_{tr} H = K_p$	${}^P_B J^T K_p {}^P_B J = K_b$
	<b>ACTUATOR</b>	<b>CONFIGURATION</b>	<b>CONTACT</b>	<b>CONTACT</b>	<b>OBJECT</b>
<b>compliance</b>	$J_a C_a J_a^T = C_q$	$J_q C_q J_q^T = C_f$	$H C_f H^T = C_{tr}$	$C_{tr} = H C_p H^T$	$C_p = {}^P_B J_b {}^P_B J^T$

condition number, resulting in a larger value of  $\sigma_1$ , indicates that the manipulability ellipsoid is closer to a sphere. This implies that the motion of the end-effector caused by joint movements is more uniform in space. On the other hand,  $\sigma_2$  represents the product of the semi-axes of the manipulability ellipsoid, and thus is proportional to the volume of the ellipsoid. A larger value of  $\sigma_2$  signifies a larger volume of the manipulability ellipsoid. Both metrics are better when larger.

The manipulability of a single finger is shown in Figure 8(A-D), where the logarithm of the condition number is normalized for better visualization. Configurations near the upper boundary generally have larger Jacobian matrix condition numbers, indicating lower manipulability. Manipulability ellipsoids for each configuration are depicted in Figures 8A and 8D. More consistent motion in Cartesian space corresponds to ellipsoids with axes of similar lengths. Near singularities (Fig. 8A), ellipsoids elongate, whereas in the center and lower part, they are more regular (Fig. 8D). If palm translation is included, the cloud can be seen as Fig. 8B shifted along the x-axis. When the left and right fingers contact, their interaction supports fine in-hand manipulation. The manipulability metric  $\sigma_2$  shows similar trends as  $\sigma_1$ . Another unresolved question mentioned in [78] is that the flexion of the index finger significantly reduces its range of adduction/abduction motion. This aligns with the results shown in Fig. 8C, where an increased flexion angle reduces the range of motion for  $S_{T_1}$  along the y-axis, resulting in a sector shape. Therefore, the issue raised in [78] is attributed to kinematic factors rather than the muscle structure of the index finger limiting the range of motion.

The overall hand manipulability,  $\sigma_2$ , normalized for visualization, is shown in Figure 9. The Jacobian matrix here is  $J \in \mathbb{R}^{3 \times 7}$ , taking into account the motion of all seven joints (two at the palm is regarded as equivalent) but only considers the translational space for visualization. The manipulability of the entire hand is the greatest at 1. It is worth noting that outside the yellow region, there should be a very thin layer with blue, which indicates the reduced manipulability at the task space boundary. In the  $\sigma_2$  manipulability cloud, 80% of the manipulability is concentrated in the range of  $0.2 \sim 0.5$ . Additionally, Figure 9A includes three graphs showing the mean distribution of manipulability. These graphs separately depict the distribution of manipulability along the  $x, y$ , and  $z$  axes. Each axis is divided into 20 intervals, with  $n$  representing the number of sampling points in each interval.

By changing the ratio of link lengths  $S_4 S_{T_1} : S_3 S_4$ , we attain different workspace and manipulability distributions (Fig. 9B). We designed the dimensions of the DexCo hand based

on experience, resulting in a workspace and manipulability similar to the human finger ratio (Fig. 9B(i)). Furthermore, based on the workspace and manipulability, we should be able to customize the DexCo hand for specific tasks in the future (Fig. 9B(i-iii)).

TABLE III  
KINEMATICS AND CONTACT INTERFACE

<b>motion</b>	$J_a \delta \theta = \delta x_f$ ( $6 \times m$ )( $m \times 1$ )( $6 \times 1$ )	$H \delta x_f = \delta x_{tr} = H \delta x$ ( $n \times 6$ )( $6 \times 1$ ) ( $n \times 1$ )( $n \times 6$ )( $6 \times 1$ )	${}^P_B J \delta x_b = \delta x_p$ ( $6 \times 6$ )( $6 \times 1$ )( $6 \times 1$ )
	<b>CONFIG</b>	<b>CONTACT</b>	<b>OBJECT</b>
<b>force</b>	$J_a^T f_f = \tau$ ( $m \times 6$ )( $6 \times 1$ )( $m \times 1$ )	$f_f = H^T f_{tr} = f_p$ ( $6 \times 1$ )( $6 \times n$ ) ( $n \times 1$ )( $6 \times 1$ )	${}^P_B J^T f_p = f_b$ ( $6 \times 6$ )( $6 \times 1$ )( $6 \times 1$ )

2) *DexCo Hand Compliance Modeling*: As the origami actuator uses soft materials as its shell, it undergoes local deformation under external force. The forcedeformation relationship of the origami actuator,  $F = g(h_0, \Delta y)$ , has been analyzed in the actuation section. In the grasping and manipulation processes, this deformation brings compliance to the DexCo hand. Compliance has been proven to simplify control in interaction tasks, as referenced in Jiang et.al. [83]. End-effector tasks, particularly fine in-hand manipulation, involve complex contact and interaction, thus emphasizing the importance of the compliance analysis. Referring to [84], the relationship between the motion transformation and force transformation of the robotic hand is shown in Table. II. In the table,  $q$  represents the displacement in the configuration space of the fingers,  $x_f$ ,  $x_{tr}$ ,  $x_p$ , and  $x_b$  are displacements in the Cartesian space:  $x_f$  is the coordinate at the contact point on the hand,  $x_{tr}$  is the part of the motion transmitted,  $x_p$  is the coordinate at the contact point on the object, and  $x_b$  is the selected external coordinate system.  $H$  is the selection matrix, and  ${}^P_B J$  is the coordinate transformation from frame  $\{P\}$  to frame  $\{B\}$ .

$K$  is the stiffness matrix under different spaces, including the actuation space  $a$ , configuration space  $q$ , cartesian space  $f, p, b$ , and transmission space  $tr$ . The assumption behind using the stiffness matrix is that the elastic force is assumed to be affine while the stiffness could be variable or nonlinear. To estimate the stiffness of an object held by the hand or the joint stiffness, we need to get the transformation from the actuator to the object or from the object back to the actuator, as shown in Table. II. In Table. II, the derivation of each column is similar. Therefore, we take the derivation process of the second column as an example, which transforms the stiffness matrix between the actuation space and the configuration space.

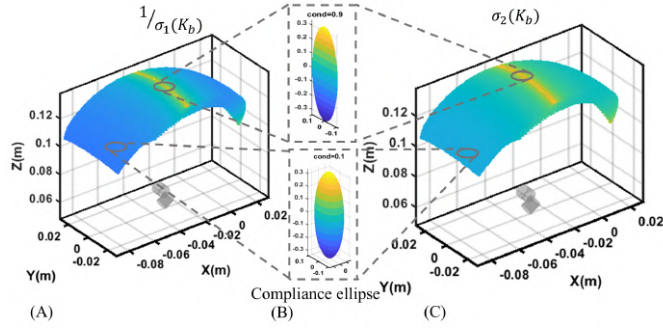


Fig. 10. Manipulability analysis and compliance analysis of a single finger. (A) Compliance cloud in cartesian space. The value at each point is attained based on the volume metric. (B) Compliance ellipse at the extremum. (C) Compliance cloud in cartesian space. The value at each point is attained based on the condition number metric. Take the logarithm of the condition number, and then normalize the result.

The same as the CONFIG column in Table. III, we attain the kinematics relation between the action space and configuration space,

$$\begin{cases} \delta q = J_a \delta a \\ J_a^T \tau = f_a \end{cases} \quad (15)$$

where  $\delta a$  is the displacement of the actuator in the actuation space,  $\delta q$  is the displacement in the configuration space,  $f_a$  denotes applied force by the origami actuator,  $\tau$  is the torque at each joint. The stiffness equations in the actuation space are:

$$\begin{cases} f_a = K_a \delta a \\ C_a f_a = \delta a \end{cases} \quad (16)$$

Combining Eq. 15 and Eq. 16 yields the transformation of the stiffness and compliance matrices between the actuation space and the configuration space, as shown in the second column of the Table. II. The transformation of the stiffness and compliance matrices between other spaces can also be obtained with the same method, based on the kinematics relation in Table. III.

The compliance analysis, similar to the manipulability analysis, is based on the 3-DoF fingers of the DexCo Hand. The metrics  $\sigma_1$  and  $\sigma_2$  are used to measure the stiffness of the fingers in space. The examples to showcase compliance analysis and the usage of stiffness transformation are separated into two cases. On one hand, we present the object stiffness in holding. On the other hand, we propose a simulator for the DexCo hand simulation in Appendix D, which makes use of the stiffness transformation in the second column of Table. II.

To determine the stiffness of the object held by the finger,  $K_b$ , the first step involves obtaining  $K_a$  and  $J_a$ . For  $K_a$ , we can assume:

$$K_a = \text{diag}([-1, -1, -1, -1]) \in \mathbb{R}^{4 \times 4} \quad (17)$$

This assumption simplifies the analysis, as the specific stiffness characteristics are not the primary focus of this analysis. Additionally, for  $J_a$ , we can also assume

$$J_a = \begin{bmatrix} 1 & 0 & 0 & 0 \\ 0 & 1 & -1 & 0 \\ 0 & 1 & 1 & 0 \\ 0 & 0 & 0 & 1 \end{bmatrix} \quad (18)$$

The matrix  $\begin{bmatrix} q_2 \\ q_3 \end{bmatrix} = \begin{bmatrix} 1 & -1 \\ 1 & 1 \end{bmatrix} \begin{bmatrix} a_2 \\ a_3 \end{bmatrix}$  in  $J_a$  describes the motion trend. When the actuator 2 and 3 at the universal joint are pressurized,  $q_2$  is not changed while  $q_3$  increases. When the actuator 2 pressurized and 3 contracted,  $q_2$  increases while  $q_3$  is not changed. This assumption also simplifies the kinematic mapping between actuation and configuration space, while the motion trend is not violated.

The compliance of a single finger is depicted in Figure 10(A~C), where the logarithm of the metric is taken and normalized.  $K_b$  represents the stiffness in the object coordinate system. Figure 10A shows the compliance cloud obtained using  $\sigma_1$ , and Figure 10C shows the compliance cloud derived from  $\sigma_2$ . Similar to manipulability, the compliance ellipsoid has a larger volume ( $\sigma_2$ ) in areas where the ellipsoid is more singular (yellow regions), as shown in Figure 10B. Additionally, it can be observed from the heatmaps of both diagrams that the variation of  $\sigma_1$  is greater than that of  $\sigma_2$ .

## V. EXPERIMENTAL VALIDATION

The objective of this section is to validate the performance of both the hardware and the proprioception system of the DexCo hand system. This validation process is composed of three distinct parts: verification at the actuator level, at the proprioception system level, and at the overall robotic hand level. Hand level validations, including grasping strength, grasping cycle time, finger strength, and finger repeatability, are referred to the benchmark [85], where these four validations are proposed. Additionally, following this benchmark, we propose the twisting strength validation to test the adduction/abduction capability of the hand. In conclusion, this section primarily introduces these experimental setups and separately discusses the results of each experiment. The key to the DexCo hand's ability to accomplish various tasks lies in its excellent performance specs, its dexterity in mimicking a human hand, and the compliance that simplifies control, as evidenced by the experimental results.

### A. Experimental System Setup

We adopted benchmarks proposed by [85] to assess the robotic hand's performance, categorizing functional indicators into grasping strength, finger strength, and grasping cycle time. In addition, to account for the hand's capability in non-planar operations, we introduced a functional indicator for torsional force inspired by the benchmark. However, the assessment of dexterity and compliance lacks a universally accepted benchmark, treated as an open question in this paper. Rather than conducting quantitative experiments for dexterity and compliance, we demonstrate these qualities practically through the hand's task completion, showcasing its compliance and dexterity in an observable manner.



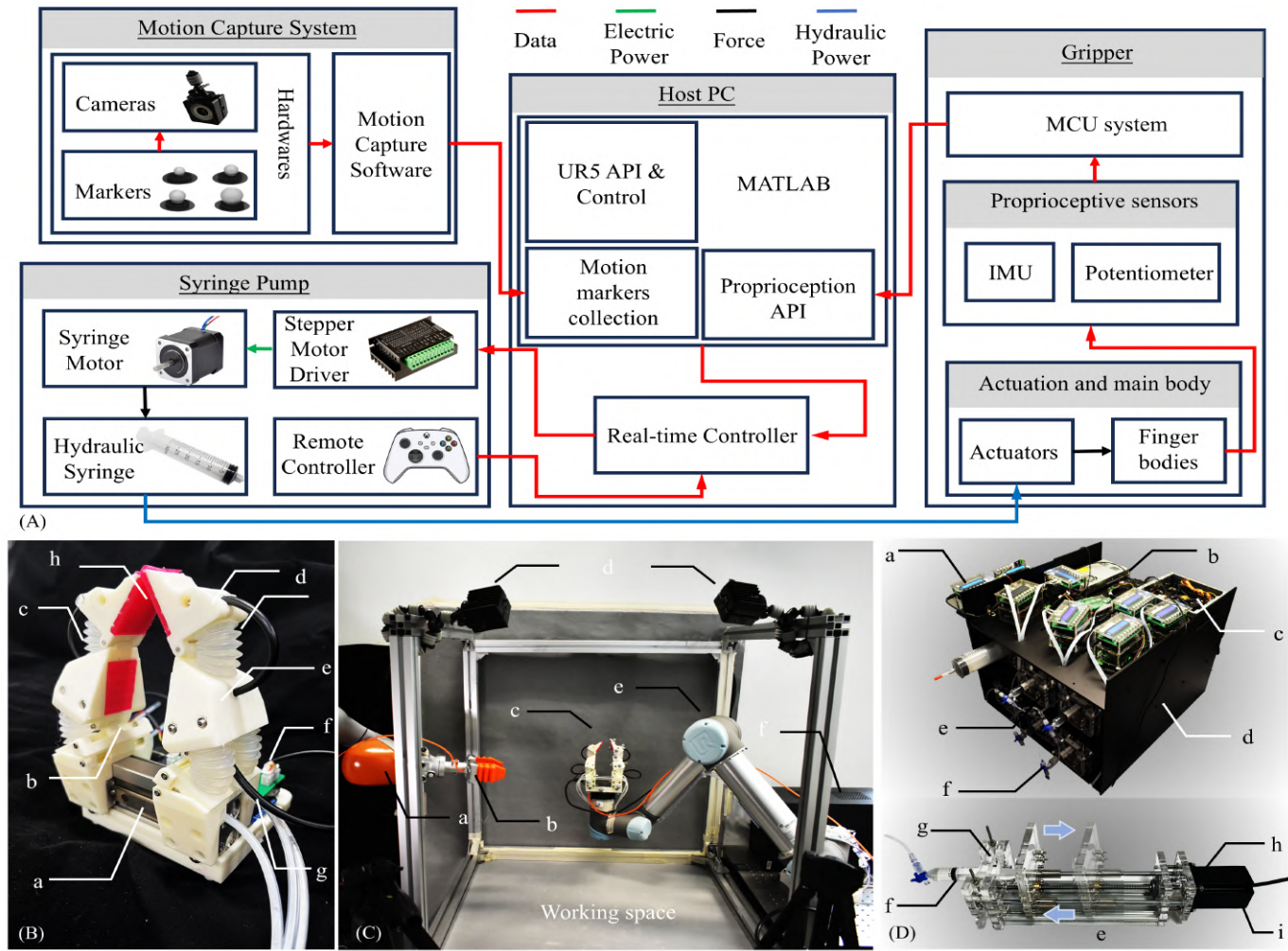


Fig. 11. System setup. (A) System blocks. (B) The DexCo hand. (a) Pneumatic palm; (b) Universal joint; (c) Hydraulic actuator; (d) 3D printed fingertip; (e) 3D printed proximal link; (f) PCB circuit and Arduino MCU; (g) IMU cable; (h) Soft pad. (C) Experimental setup. (a) KUKA iiwa arm; (b) A normal soft gripper; (c) The DexCo hand; (d) Cameras of the motion capture system (Optitracker); (e) UR 5 arm; (f) Host PC. (D) The syringe pump system. (a) Stepper motor driver; (b) 24V DC power; (c) Stepper motor controller; (d) Acrylic syringe pump box; (e) Syringe pump; (f) Hydraulic syringe; (g) Syringe locker; (h) Stepper motor; (i) Electromagnetic encoder.

The experimental setup encompasses three platforms: the actuator platform, the proprioception system platform, and the robotic hand test platform. The experimental platform is illustrated in Fig. 11A and 11C. The platform consists of five components: a motion capture system, a syringe pump system, a UR5 system, the robotic hand system, and a host computer (Fig. 11A). Reflective markers on each link of the robotic hand, captured by motion cameras in the Optitrack system, enable the calculation of the hand's configuration space. The syringe pump system, with eight independent pumps, controls actuator expansion and contraction directly, with data collection and transmission to the host computer. The robotic hand, equipped with origami actuators, IMUs, linear potentiometers, Arduino, and peripheral circuits, communicates configuration space information to the host computer. Data collection and high-level control commands, such as UR5 movement positions and finger speed, are facilitated through MATLAB interfaces.

The actuator testing platform comprises a single-channel

syringe pump (Fig. 11D), an origami actuator, a linear guide, and a force sensor. DexCo hand-related tests involve the UR5, DexCo hand (Fig. 11B), two single-axis force sensors (Fig. 13B), a six-axis sensor, and a data acquisition card.

### B. Hydraulic Actuator Local Compliance Validation

In this experiment, the origami actuators are locked in the same way as in the robotic hand, with one end fixed to a uniaxial force sensor and the other end to a linear slide. The hydraulic actuators are connected to the syringe pump, simulating the state of the actuators under actuation. During the experiment, the syringe pump drives the origami actuator from its shortest length to its maximum length (23 mm ~ 33.5 mm), with each interval being 1.5 mm (as shown in Fig. 6H). At each driven length, the linear slide stretches and compresses the actuator within a range that does not cause severe yielding, with a total displacement of about 30 mm and an incremental displacement of 1 mm each time. This reciprocating test was repeated three times, and the average

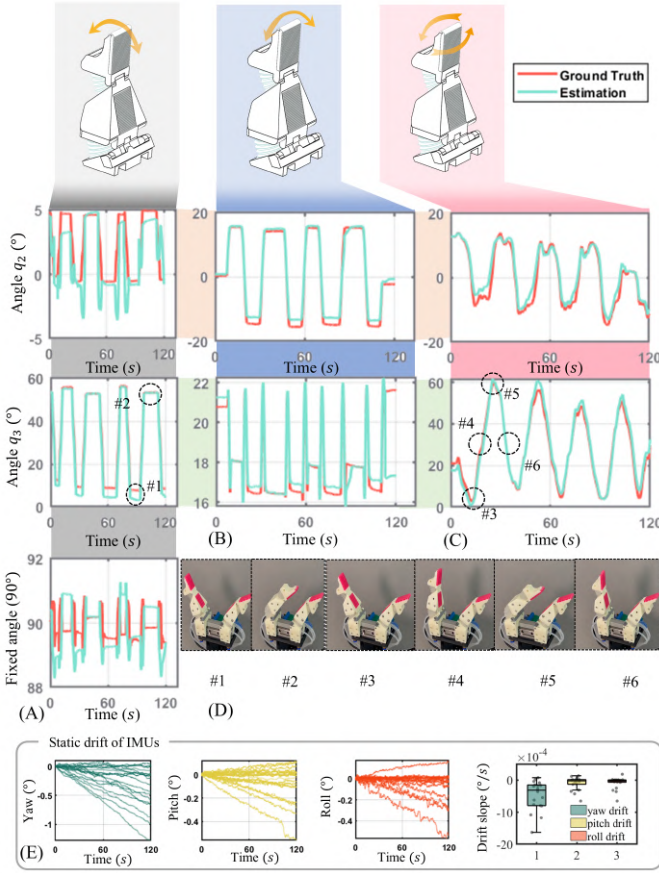


Fig. 12. Position feedback of IMU in all motions. (A) Position feedback in flexion of the proximal link. The constant angle,  $90^\circ$ , has small variants (about  $2^\circ$ ) in the solution. (B) Position in adduction/abduction of the proximal link. The jumping change happens due to the collision between the proximal link and base link. (C) Position feedback in normal motion. (D) Hand Motions. Pose #1 and #2 fit with the time of  $q_3$  figure in (A). Pose #3~#6 fit with the time of  $q_3$  figure in (C). (E) IMU drift in static and the drift slope distribution.

force at each position was used as the measure of force exerted at that position.

As shown in Figure 6H, the range of force exerted by the actuator lies between  $-122.4$  N and  $27.4$  N. The longer the actuator (higher  $h_0$ ), the weaker its ability to be stretched positively; conversely, the shorter the actuator, the weaker its ability to be compressed. The bottom of Figure 6H shows the difference between theoretical and actual forces, denoted as  $|\Delta F|$ . This difference is greatest near  $h_0 = 23$  mm, primarily because, at this length, the actuator has the most prominent unexpected deformation on the origami shell.

### C. Proprioception Validation

In this experiment, we conducted tests focusing on both stability and accuracy. In the accuracy experiment, we gathered sensor data and motion capture system data while the DexCo hand assumed different postures. The motion capture system provided spatial pose data for the finger link, serving as the ground truth for the robotic hand's posture. The configuration space of the robotic hand was calculated based on Equation 5. We collected ground truth and IMU data five times for each posture, averaging the values. The average values were

### Algorithm 1 Steps for Grasp Strength Validation

**Require:**  $A_s, G_{\text{type}}, q_{\text{init}}, \rho_0$   $\triangleright$  artifact size, grasp type, initial joint position of the hand, number of cycles  
1:  $q \leftarrow \text{config}(G_{\text{type}}, A_s)$   $\triangleright$  desired joint angles  
2:  $\rho \leftarrow 0$   $\triangleright$  current grasp cycle  
3: **while**  $\rho_0 - \rho > 0$  **do**  
4:    $\text{hand.goto}(q_{\text{init}})$   $\triangleright$  fully open the hand  
5:    $\text{hand.goto}(q)$   $\triangleright$  fully close the hand  
6:    $\text{wait}(t_s)$   $\triangleright$  stabilize force data  
7:    $f \leftarrow \text{sensor.observe}(\text{mean}())$   $\triangleright$  collect force  
8:    $\rho \leftarrow \rho + 1$   $\triangleright$  update grasp cycle  
9: **end while**

then converted to the robotic hand's configuration space for comparison, allowing us to assess the accuracy of the IMU in estimating the dexterous hand's posture. Further details on the calibration method between the IMU and ground truth can be found in Appendix A.

The DexCo hand performed three representative actions: flexion, adduction/abduction, and mixed. Results displayed in Figure 12(A ~ C) indicate the IMU's accuracy is commendable, with a deviation in configuration space ranging approximately from  $0^\circ$  to  $5^\circ$ , depending on the situation. Notably, in Figure 12A, where the expected result is  $90^\circ$ , some fluctuations are observed. This is attributed to the use of an optimization-based calibration method, introducing slight deviations.

The stability experiment focuses on the IMU data drift. Employing the same setup as the accuracy experiment, the DexCo hand maintained stillness in various posture while two-minute data is collected for each posture (Fig. 12E). The distribution of the drift slope is shown in Fig. 12E, where the average drift slope is  $[-0.49, -0.10, -0.09] \times 10^{-3}$  for yaw pitch and roll. The residual sum of squares,  $\sum (y - y_{\text{fit}})^2$ , which can be used to describe the data drift stability, is  $[0.64, 0.08, 0.20]$  degrees for yaw pitch and roll. Overall, based on our experience, utilizing the system for up to ten minutes during manipulation poses no issues.

### D. Grasping Strength Validation

Grasp strength serves as a crucial indicator of a robotic hand's capability to apply maximum force to an object. For the experiment, 3D-printed artifacts were split into two parts to facilitate both pinch and wrap grasps. Pinch grasp tests utilized five block-shaped artifacts, while wrap grasp tests involved four cylindrical artifacts. Force sensors were secured with rubber bands at both ends to prevent shear forces. As shown in Algorithm 1, given the artifact size and grasp type, position control was applied to the hand to reach the desired configuration, where the number of cycles  $\rho$  is 32 in the experiment.

To ensure accuracy, the sum of force readings from each tandem pressure sensor was taken. A quasi-static grasp force was employed to determine the true strength of the end-effector, disregarding the first and last 10% of non-zero data in each cycle. The remaining middle 80% was used to calculate



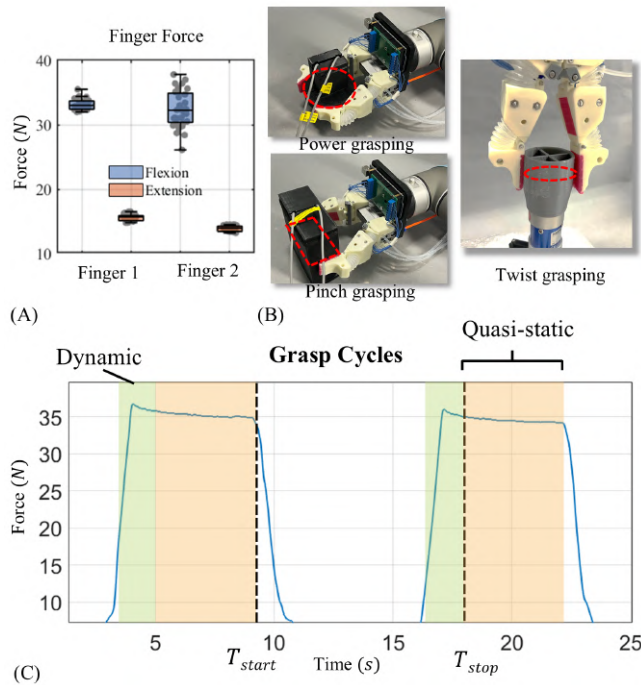


Fig. 13. (A) The finger strength experiment. Finger 1 is finger in good condition. Finger 2 is finger with air in hydraulic actuator. (B) Experiment setup in tests, including grasping strength, grasp cycle time, repeatability, and twisting strength. A rectangular box is grasped in pinch test. A cylindrical box is grasped in power grasping test. (C) Force-time pattern in grasping strength and grasp cycle time experiments.

TABLE IV  
THE GRASP STRENGTH OF DIFFERENT GRASP TYPES AND ARTIFACT SIZE DIMENSIONS

Grasp type	Artifact size (mm)	Avg total force(N)	Stdev (N)	95% confidence interval (N)
Power	40	27.16	1.97	[26.45, 27.87]
	55	26.31	2.30	[25.48, 27.14]
	70	24.10	1.76	[23.47, 24.73]
	85	24.83	1.77	[24.19, 25.47]
Pinch	35	20.14	1.55	[19.13, 19.99]
	60	21.31	2.08	[20.22, 22.40]
	85	22.40	0.87	[21.36, 23.43]
	110	29.26	1.88	[28.29, 30.23]
	120	38.24	2.70	[37.24, 39.24]

the average combined force ( $F_{total}$ ). Mean, standard deviation, and 95% confidence interval were calculated based on the average of all 32 cycles.

Table IV presents the grasp strength results for different grasp types and artifact size dimensions. Power grasping strength remained relatively consistent across artifact sizes, whereas pinch grasp strength increased with larger artifact sizes. Notably, power grasping exhibited higher strength than pinch grasping (20.14N to 22.4N) for the same size, ranging from 24.83N to 27.16N, attributed to a significant portion of the grasping strength being directed in the shear direction during power grasp tests. Additionally, a downward trend in grasp strength during cycling indicates potential durability testing may be required for this end-effector.

TABLE V  
THE GRASP CYCLE FOR DIFFERENT GRASP TYPES AND ARTIFACT SIZE DIMENSIONS

Grasp type	Artifact size (mm)	Avg cycle time (s)	Stdev (s)	95% confidence interval (s)
Power	40	1.40	0.09	[1.37, 1.43]
	55	1.36	0.15	[1.30, 1.41]
	70	1.39	0.06	[1.37, 1.41]
	85	1.33	0.14	[1.28, 1.38]
Pinch	35	2.04	0.10	[2.00, 2.07]
	60	1.59	0.04	[1.57, 1.60]
	85	1.41	0.05	[1.40, 1.43]
	110	1.13	0.08	[1.10, 1.16]
	120	1.02	0.06	[1.00, 1.04]

### E. Grasping Cycle Time Validation

Grasp cycle time is the time taken by a robotic hand to close and open from a pre-grasp configuration to a grab position and back. The experiment setup and procedure for conducting the grasp cycle time test is the same as the grasp force test (Algorithm 1). The grasp cycle begins when the end-effector begins to close from a fully open initial attitude and ends when the finger is opened after the grasp has been performed. The  $T_{cycle}$  is defined by two adjacent cycles,  $T_{start}$  and  $T_{stop}$ , as shown in Figure 13C, where  $T_{start}$  marks the time when the quasi-static force is removed from the artifact at the end of each grasp, and  $T_{stop}$  occurs at the point in time when the dynamic force has stabilized to a quasi-static.

The grasp cycle time for every individual grasp was computed using the equation  $T_{cycle} = T_{stop} - T_{start}$ . The grasp cycle time data for nine artifacts were compared for both grasp types of our end-effector, as shown in Table V. Irrespective of the type of grasp, there exists a correlation between artifact size and the grasp cycle time, wherein the cycle time tends to decrease as artifact size increases. However, it is noteworthy that the pinch test (1.02s to 2.04s) exhibits a more pronounced decreasing trend in cycle time as compared to the wrap test (1.33s to 1.40s).

### F. Finger Strength Validation

Our methodology for measuring finger force is similar to the previous experimental setup. Each finger pushes against a pinch box (Figure 13B), while the pinch box is securely anchored to the ground in this test. The procedure entailed a series of standardized steps executed for each finger (Algorithm 2). Given the finger type and motion type, position control was applied to the hand to reach the desired configuration. Similar to the grasp strength validation, the DexCo hand was instructed to repeatedly fully open and close, and mean force is collected in a quasi-static period, with  $\rho$  set as 32 and  $t_s$  set as five seconds.

Finger 1 is newly manufactured; Finger 2 is heavily used for two days. The most prominent difference between fingers 1 and 2 is the air bubbles in the hydraulic actuator. In the hydraulic actuator of finger 2, one-sixth of the volume is empty in a fully extended state. Therefore, the comparison of fingers 1 and 2 shows the effect of air bubbles on hydraulic actuators and indicates the difference between hydraulic actuation and pneumatic actuation. Table VI and Figure 13A



### Algorithm 2 Steps for Finger Strength Validation

**Require:**  $F_{\text{type}}, M_{\text{type}}, q_{\text{init}}, \rho_0$   $\triangleright$  finger type, motion type, initial joint position of the hand, number of cycles

- 1:  $q \leftarrow \text{config}(F_{\text{type}}, M_{\text{type}})$   $\triangleright$  desired joint angles
- 2:  $\rho \leftarrow 0$   $\triangleright$  current cycle
- 3: **while**  $\rho_0 - \rho > 0$  **do**
- 4:    $\text{hand.goto}(q_{\text{init}})$   $\triangleright$  fully open the hand
- 5:    $\text{hand.goto}(q)$   $\triangleright$  fully close the hand
- 6:    $\text{wait}(t_s)$   $\triangleright$  stabilize force data
- 7:    $f \leftarrow \text{sensor.observemean}()$   $\triangleright$  collect force
- 8:    $\rho \leftarrow \rho + 1$   $\triangleright$  update grasp cycle
- 9: **end while**

TABLE VI  
THE FINGER STRENGTH DATA FOR TWO FINGERS WITH DIFFERENT MOTION TYPES

Finger	Motion types	Avg finger strength (N)	Stdev (N)	95% confidence interval (N)
1	Flexion	34.83	0.80	[34.54, 36.12]
	Extension	15.64	0.46	[15.48, 15.81]
2	Flexion	34.43	2.75	[33.44, 35.43]
	Extension	13.88	0.41	[13.73, 14.03]

show the strength performance of two fingers. Firstly, the air bubbles have little effect on the maximum average finger force. However, in the experiment, finger 2 requires a larger displacement to reach the maximum finger force (34.43N for flexion and 13.88N for extension). Secondly, the air bubbles greatly enlarge the standard deviation. This could be because of the reduced finger precision when there are bubbles in hydraulic actuators.

### G. Finger Repeatability Validation

Finger repeatability measures how consistently a finger can reach the same position from the same direction. The accuracy of finger repeatability is tested using a linear displacement sensor that provides unidirectional measurement accuracy of 0.02 mm. The test requires the finger to move to four unique positions before returning to the starting position, covering most of the finger's workspace. As shown in the Algorithm 3,  $q_a, q_b, q_c$ , and  $q_{\text{init}}$  are completely disengaged by actuating each joint. Number of cycles  $\rho$  is 32 in the experiment.

TABLE VII  
THE FINGER REPEATABILITY

Finger	Avg offset distance (mm)	Stdev (mm)	95% confidence interval (mm)
1	-0.03	0.08	[-0.06, 0.00]
2	-0.69	0.43	[-0.85, -0.54]

TABLE VIII  
TWIST STRENGTH FOR DIFFERENT SIZED OBJECTS

Artifact size (mm)	Avg torque (Nm)	Stdev (Nm)	95% confidence interval (Nm)
30	0.082	0.016	[0.076, 0.088]
50	0.229	0.038	[0.215, 0.242]
70	0.428	0.058	[0.407, 0.449]
90	0.587	0.050	[0.579, 0.615]

### Algorithm 3 Steps for Finger Repeatability Validation

**Require:**  $F_{\text{type}}, q_{\text{init}}, \rho_0$   $\triangleright$  finger type, initial joint position of the hand, number of cycles

- 1:  $q_a, q_b, q_c \leftarrow \text{config}(F_{\text{type}})$   $\triangleright$  three different desired joint angles
- 2:  $\rho \leftarrow 0$   $\triangleright$  current cycle
- 3: **while**  $\rho_0 - \rho > 0$  **do**
- 4:    $\text{hand.goto}(q_{\text{init}})$
- 5:    $d_0 \leftarrow \text{sensor.observe}()$   $\triangleright$  initial displacement
- 6:    $\text{hand.goto}(q_a)$
- 7:    $\text{hand.goto}(q_b)$
- 8:    $\text{hand.goto}(q_c)$
- 9:    $\text{hand.goto}(q_{\text{init}})$   $\triangleright$  back to initial configuration
- 10:    $d \leftarrow \text{sensor.observe}()$   $\triangleright$  final displacement
- 11:    $\rho \leftarrow \rho + 1$   $\triangleright$  update grasp cycle
- 12:    $\text{offset} \leftarrow \text{abs}(d - d_0)$   $\triangleright$  offset in current cycle
- 13: **end while**

### Algorithm 4 Steps for Twist Strength Validation

**Require:**  $A_s, q_{\text{init}}, \rho_0$   $\triangleright$  artifact size, initial joint position of the hand, number of cycles

- 1:  $q \leftarrow \text{config}(A_s)$   $\triangleright$  desired joint angles for fully close
- 2:  $\theta \leftarrow \text{trajectory}(A_s)$   $\triangleright$  joint trajectory for twist
- 3:  $\rho \leftarrow 0$
- 4: **while**  $\rho_0 - \rho > 0$  **do**
- 5:    $\text{hand.goto}(q_{\text{init}})$   $\triangleright$  fully open the hand
- 6:    $\text{hand.goto}(q)$   $\triangleright$  fully close the hand
- 7:    $\text{hand.execute}(\theta)$   $\triangleright$  perform twist motion
- 8:    $\text{wait}(t_s)$   $\triangleright$  stabilize torque data
- 9:    $\tau \leftarrow \text{sensor.observemean}()$   $\triangleright$  collect torque
- 10:    $\rho \leftarrow \rho + 1$   $\triangleright$  update grasp cycle
- 11: **end while**

Finger 1, with a 0.03mm repeatability accuracy, demonstrates performance closely aligned with that of a conventional rigid hand (Tab. VII), thereby exhibiting better repeatability compared to Finger 2 (0.69mm repeatability accuracy).

### H. DexCo Hand Twisting Strength Validation

Based on the existing benchmarks [85], we introduce the twist strength benchmark to evaluate robotic hands. The twist strength of a robotic hand refers to the highest amount of torque generated by the pinch grasp (Fig. 13B). The torque sensor's rotational axis was oriented perpendicular to the palm during a pinch grasp. As shown in Algorithm 4, the DexCo hand is firstly instructed to its fully open configuration. Then, fingers are commanded to the fully close state, such that the hand achieves a maximum grasp force before twisting. Finally, the DexCo hand implements the twisting motion  $\theta$  at this maximum pinch force to measure the maximum torque under quasi-static conditions, where  $\theta$  is any angle that ensures the hand twists to achieve the maximum torque.  $t_s$  is set as five seconds and  $\rho$  is 32 in this experiment.

We designed four artifacts to be mounted on the torque sensor. For each set of torque readings obtained from the torque sensor, the stabilized torque under quasi-static conditions was calculated for each cycle, as presented in Table VIII.

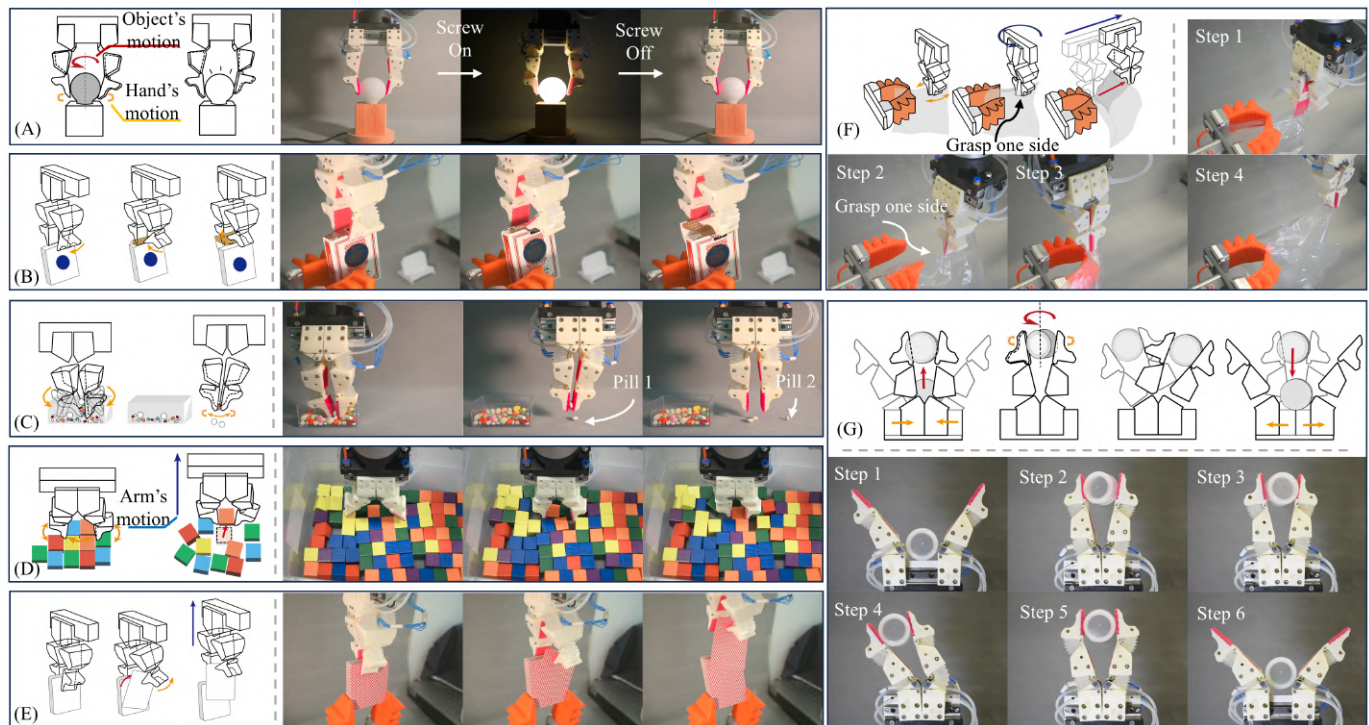


Fig. 14. Fine in-hand manipulation demonstration. (A) Screw On and Screw Off a real light bulb. (B) Card box opening. (C) Picking and sorting pills based on size with in-finger manipulation. (D) Cluttered bin picking with finger-environmental interaction. (E) Counting Cards and taking card out one by one. (F) Plastic bag opening. (G) Typical caging manipulation and in-hand rotation.

## VI. DEXCO HAND FINE IN-HAND MANIPULATION

The DexCo hand has successfully achieved advanced manipulation capabilities across a range of fine in-hand tasks. Beyond typical pinch and power grasps, it excels in challenging scenarios such as cluttered picking, assembling light bulbs, and unscrewing bottle caps, even in constrained environments. Additionally, it has succeeded in tasks previously unattainable by other dexterous hands, including opening plastic bags, counting cards, and sorting medications, highlighting its versatility in fine manipulation. Figure 14 showcases these diverse tasks, consistent with the previously referenced material:

**The light bulb assembly task** (Figure 14A) involves tightening and then unscrewing the bulb using the DexCo hand's forward and backward twisting motions. To demonstrate its compliance, the hand's central axis is offset from the bulb's axis on the xy plane. A wider palm requires greater joint flexion to grip the object, and as flexion increases, the y-axis motion range decreases. The palm's width adjusts the twisting range accordingly.

**Card box opening** task is shown in Figure 14B. The box's top end has a semi-circular opening, typically opened by inserting fingers. The DexCo hand employs a similar mechanism, opening the box from above using its flexion DoFs or the side using its adduction/abduction DoFs. During this process, the robot arm remains stationary.

**Pill sorting** is depicted in Figure 14C. The process includes picking multiple pills from a pile and then categorizing them into different piles using fine in-hand manipulation. This task requires the DexCo hand to utilize its fingertip dexterity to pick a portion of the pills from a cluttered arrangement, followed

by separating the small particles using fingertip sliding, akin to the human hand sprinkling powder.

**Cluttered bin picking** (Fig. 14D) features dense hand-environment interaction, which is a great challenge for robots to operate in an unstructured environment. In the real world, pick and place is not enough because objects are always stacked or gathered in a confined space. From our result, the dexterity at the fingertip of the DexCo hand demonstrates a great capability to manipulate in clutter. We believe that the manipulation for grasping capability of the DexCo hand can solve this cluttered bin picking challenge.

**Card-counting** task is illustrated in Figure 14E. Human hands use the thumb and index finger to swiftly extract cards from a deck, with the other hand assisting. The DexCo hand mimics this, with the orange soft hand holding the deck for assistance. The DexCo hand uses its fingertip dexterity to first separate the top card, with no arm movement. Once the card is separated, the arm moves upwards to extract it. Without this fine in-hand manipulation, consecutive cards would be removed together.

**Opening a plastic bag** is shown in Figure 14F. The soft orange hand, attached to the end of a KUKA robot, adjusts its opening and closing through pneumatic control. This task involves initially manipulating the unopened, transparent, thin plastic bag with the fingertips to open it and grip one edge. The bag is then repositioned for the soft hand to grasp the other edge, and the DexCo hand pulls it open. The success of the bag-opening phase depends on the dexterity and compliance of the fine in-hand manipulation. During the bag-stretching phase, sufficient gripping force is required while pinching with

the DexCo hand.

**Caging manipulation and in-hand rotation.** Figure 14G, depicts two sliding primitives along the x and y axes and two translation primitives along the y and z axes, as classified by Dollar et al. (2014) [1]. The palm's role here is to extend the range of sliding, perform translational movement, and accommodate a wider range of object diameters. The hand's local compliance also increases the safety margin during manipulation, reducing control difficulty.

## VII. CONCLUSION AND FUTURE WORK

This study has introduced the Dexterous and Compliant (DexCo) hand system, which successfully mimics human fine in-hand manipulation capabilities. By leveraging soft hydraulic actuation, the DexCo hand achieves a balance between control complexity, dexterity, compliance, and motion accuracy. Experimental results have demonstrated its ability to perform complex tasks such as screwing light bulbs, opening plastic bags, and counting cards, showcasing its versatility in real-world applications. The integration of soft actuation and proprioceptive feedback allows for more nuanced and precise manipulation, addressing challenges that have long hindered the field of robotics. The DexCo hand's compact and compliant design holds great promise for advancing the capabilities of robotic systems in a range of environments, from industrial settings to everyday tasks.

Future research will focus on enhancing the DexCo hand's ability to autonomously perform a broader range of tasks, particularly in unstructured environments. Improving the integration of sensory feedback for real-time adjustments and more delicate object handling will be a key objective. Additional efforts will be made to optimize the hand's design for greater durability and energy efficiency in repetitive or continuous operations. Investigating machine learning algorithms to enable the DexCo hand to self-adapt to varying task demands will further extend its capabilities, allowing for more intelligent manipulation strategies. Lastly, expanding its applications in sectors such as healthcare, manufacturing, and service industries will be explored to fully leverage the system's potential.

### APPENDIX A IMU CALIBRATION METHOD

A complete rigid body calibration system is shown in Fig. 15A, which includes the current pose of IMU denoted as  $\{I\}$ , the current pose of ground truth sensor denoted as  $\{r\}$ , the body-fixed frame  $\{b\}$ , the initial frame of IMU denoted as  $\{I_0\}$ , the initial frame of ground truth sensor denoted as  $\{r_0\}$ , and the world frame denoted as  $\{g\}$ . The frames  $\{I\}$ ,  $\{r\}$  and  $\{b\}$  are attached to the rigid body, while the frames  $\{I_0\}$ ,  $\{r_0\}$  and  $\{g\}$  are attached to the ground. The representation of  $\{I\}$  and  $\{r\}$  in  $\{g\}$  is shown as follows:

$$\begin{cases} {}^g\tilde{R}_b \cdot {}^bR_I = {}^g\tilde{R}_I \\ {}^g\tilde{R}_b \cdot {}^bR_r = {}^g\tilde{R}_r \end{cases} \quad (19)$$

The calibration objective is to find the transformation relationship between  ${}^g\tilde{R}_I$  and  ${}^g\tilde{R}_r$ . Without sacrifice of generality, we make the following two substitutions:

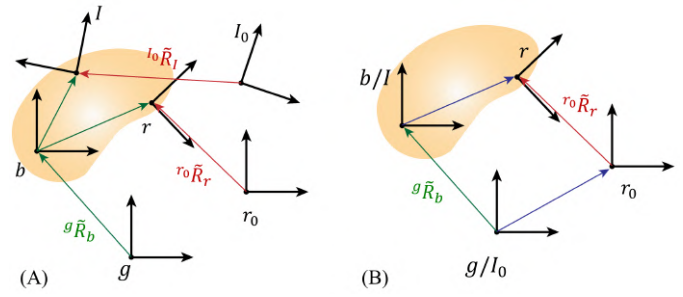


Fig. 15. (A) Frames of the rigid body. (B) The substituted frames of the rigid body.

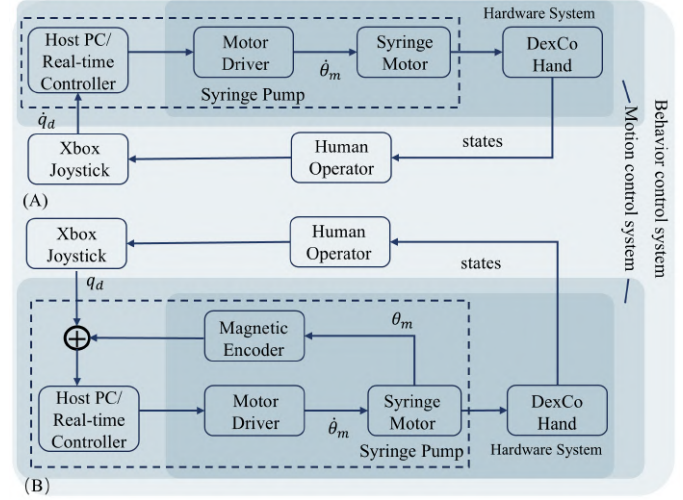


Fig. 16. Hierarchical control blocks. (A) Teleoperated joint velocity control of the DexCo hand. (B) Teleoperated joint position control of the DexCo hand.

- *Assumption 1:* let  $\{g\} = \{I_0\}$ , i.e.  ${}^gR_{I_0} = I$ ;
- *Assumption 2:* let  $\{b\} = \{I\}$ , i.e.  ${}^gR_I = I$ .

We can simplify the coordinate system as shown in the Figure 15B. Moreover, we can obtain

$${}^g\tilde{R}_b \cdot {}^bR_r = {}^gR_{r_0} \cdot {}^{r_0}\tilde{R}_r \quad (20)$$

Our goal is to collect IMU and ground truth data from two different positions,  ${}^g\tilde{R}_b, {}^{r_1}\tilde{R}_{r_0}$  and  ${}^g\tilde{R}_b, {}^{r_2}\tilde{R}_{r_0}$  respectively, to obtain two parameter matrices,  ${}^bR_r$  and  ${}^gR_{r_0}$ . We have

$${}^g\tilde{R}_b \cdot {}^bR_r \cdot {}^{r_1}\tilde{R}_{r_0} = {}^g\tilde{R}_b \cdot {}^bR_r \cdot {}^{r_2}\tilde{R}_{r_0} \quad (21)$$

To obtain  ${}^bR_r$ , we formulate the above equation as a nonlinear optimization problem.

$$\begin{aligned} \text{Minimize: } & f(R) = \left\| R \cdot {}^{r_1}\tilde{R}_{r_0} \cdot {}^{r_2}\tilde{R}_{r_0} - {}^g\tilde{R}_b \cdot {}^g\tilde{R}_b \cdot R \right\|_F \\ \text{Subject to: } & R^T \cdot R = I, \\ & \det(R) = 1; \end{aligned}$$

In this context,  $\|\cdot\|_F$  denotes the Frobenius norm. By employing this optimization approach, it is possible to find  ${}^bR_r$  and  ${}^gR_{r_0}$  that closely approximate the ground truth values.



## APPENDIX B ELLIPSE IN MATRIX

Considering a matrix  $A$  below,

$$\begin{bmatrix} x \\ y \end{bmatrix}^T \begin{bmatrix} 5 & 4 \\ 4 & 5 \end{bmatrix} \begin{bmatrix} x \\ y \end{bmatrix} = x^T A x = 1 \quad (22)$$

where  $A$  is a positive-definite matrix. The eigenvalues are  $\lambda_1 = 1, \lambda_2 = 9$ , and the normalized eigenvectors are  $\mu_1 = \begin{bmatrix} \frac{1}{\sqrt{2}} \\ \frac{1}{\sqrt{2}} \end{bmatrix}, \mu_2 = \begin{bmatrix} \frac{1}{\sqrt{2}} \\ -\frac{1}{\sqrt{2}} \end{bmatrix}$ . We can then decompose  $A$  orthogonally,

$$A = Q \Lambda Q^{-1} = Q \Lambda Q^T$$

$$= \begin{bmatrix} \frac{1}{\sqrt{2}} & \frac{1}{\sqrt{2}} \\ -\frac{1}{\sqrt{2}} & \frac{1}{\sqrt{2}} \end{bmatrix} \begin{bmatrix} 1 & 0 \\ 0 & 9 \end{bmatrix} \begin{bmatrix} \frac{1}{\sqrt{2}} & -\frac{1}{\sqrt{2}} \\ \frac{1}{\sqrt{2}} & \frac{1}{\sqrt{2}} \end{bmatrix} \quad (23)$$

where

$$P(f) = x^T A x = x^T Q \Lambda Q^T x$$

$$= (Q^T x)^T \Lambda (Q^T x)$$

$$= 1 \left( \frac{x-y}{\sqrt{2}} \right)^2 + 9 \left( \frac{x+y}{\sqrt{2}} \right)^2 \quad (24)$$

The relationship between the axes of an ellipse and the eigenvectors of the matrix  $A$  can be observed. the length of the semi-axis can be calculated as the square of the inverse of the eigenvalue of  $A$ .

## APPENDIX C TELEOPERATED CONTROL FOR VARIOUS TASKS

The DexCo hand is teleoperated to accomplish the manipulation tasks, rather than hard coding. An Xbox joystick can intuitively control 7 dofs of the DexCo hand, including 6 dofs for the motion of 2 fingers and 1 dofs for the plam motion and stiffness. In this paper, we implemented two controllers controlling the position (Fig. 16B) and velocity (Fig. 16A) of the hand.

For the velocity control, as shown in Fig. 16A, the joystick sends out the desired velocity commands,  $\dot{q}_d$ , to the real-time controller, which is a PID controller with an inverse kinematic computation based on Eq. 18. The syringe motor is controlled in an open-loop under velocity control mode. Pressed button represents a fixed velocity, while the stick and trigger map to a continuous velocity range.

For the position control, as shown in the Fix. 16B, the joystick sends the desired position commands,  $q_d$ , to the real-time controller, where a PID controller takes in the error and sends the control output  $\dot{\theta}_m$ . By using a magnetic encoder for feedback, we can control the stepper motor at a high frequency. In the position control mode, the stick space,  $[-1, 1] \in \mathbb{R}^2$ , and trigger space,  $[0, 1] \in \mathbb{R}$ , are mapped to a specific position of the joint.

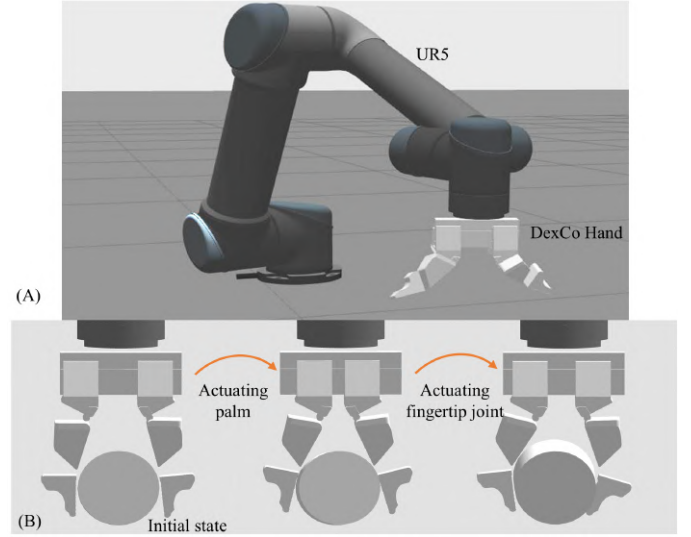


Fig. 17. Simulator for DexCo hand. (A) Integration with UR5. (B) Illustration of active motion and passive compliance in simulator.

## APPENDIX D SIMULATOR FOR DEXCO HAND WITH SOFT HYDRAULIC ACTUATION MECHANISM

We implement the DexCo hand as a ROS package for simulation, which could also be treated as a case study for compliance modeling. Based on Eq. 18, we substitute the parameters in Jacobian with the kinematics structure

$$\begin{bmatrix} q_1 \\ q_2 \\ q_3 \\ q_4 \end{bmatrix} = \begin{bmatrix} 1 & 0 & 0 & 0 \\ 0 & 37 & -37 & 0 \\ 0 & 33.3 & 33.3 & 0 \\ 0 & 0 & 0 & 66.7 \end{bmatrix} \begin{bmatrix} h_1 \\ h_2 \\ h_3 \\ h_4 \end{bmatrix} = J_a h \quad (25)$$

where  $h$  represents the actuation space for one finger. Based on the Jacobian, we can easily transform the motion, force, and linear stiffness between the configuration space  $q$  and actuation space  $h$ , as shown in Table II and III. The variable stiffness property inherent in the DexCo hand can be modeled as linear elastic force or nonlinear elastic force as shown below

$$\tau_k = -k(q_0) \Delta q \quad (26)$$

$$\tau_k = f(q_0, \Delta q) \quad (27)$$

where  $q_0$  is the joint angle without external force,  $q$  is the current joint angle,  $\Delta q = q - q_0$  represents the current deformation. The linear elastic force, Eq. 26, can be transformed based on the stiffness matrix,  $K_a = J_a^T K_q J_a$ . The nonlinear elastic force, Eq. 27, which is more accurate in describing the motion of the DexCo hand, cannot be directly transformed using the stiffness matrix.

By modeling the stiffness as force in simulation, it should affect the dynamics in simulation as the following way

$$M \ddot{q} + H(\dot{q}, q) = \tau_k \quad (28)$$

where the left-hand side represents the terms of inertial force, Coriolis force, and gravity, which are developed by

the simulator, while the right-hand side represents the torques at the joints.  $\tau_k$  is the torque generated from deformation. Implementing the torque  $\tau_k$ , we can successfully simulate the behavior of the nonlinear, variable stiffness elastic force.

Fig. 17A shows the simulator in gazebo. The UR5 can be automatically controlled by moveit, while the DexCo hand is controlled by joint position signals. It is worth noting that the simulator of DexCo hand fully simulates the hydraulic position control in actuation space by treating it as variable stiffness relation (Eq. 26 or 27). Fig. 17B presents the nonlinear variable stiffness property in grasping and manipulating a cylinder. The palm is firstly commanded to close without actuating other joints, where those joints adapt to the object. Then, the fingertip is actuated for further manipulation.

## REFERENCES

- [1] A. M. Dollar, "Classifying human hand use and the activities of daily living," *The human hand as an inspiration for robot hand development*, pp. 201–216, 2014.
- [2] A. Billard and D. Kragic, "Trends and challenges in robot manipulation," *Science*, vol. 364, no. 6446, p. eaat8414, 2019.
- [3] A. Bicchi, "Hands for dexterous manipulation and robust grasping: A difficult road toward simplicity," *IEEE Transactions on robotics and automation*, vol. 16, no. 6, pp. 652–662, 2000.
- [4] M. R. Cutkosky et al., "On grasp choice, grasp models, and the design of hands for manufacturing tasks," *IEEE Transactions on robotics and automation*, vol. 5, no. 3, pp. 269–279, 1989.
- [5] S. Puhlmann, J. Harris, and O. Brock, "Rbo hand 3: A platform for soft dexterous manipulation," *IEEE Transactions on Robotics*, vol. 38, no. 6, pp. 3434–3449, 2022.
- [6] A. S. Morgan, K. Hang, B. Wen, K. Bekris, and A. M. Dollar, "Complex in-hand manipulation via compliance-enabled finger gaiting and multimodal planning," *IEEE Robotics and Automation Letters*, vol. 7, no. 2, pp. 4821–4828, 2022.
- [7] A. Bhatt, A. Sieler, S. Puhlmann, and O. Brock, "Surprisingly robust in-hand manipulation: An empirical study," *arXiv preprint arXiv:2201.11503*, 2022.
- [8] J. Zhou, X. Chen, U. Chang, J.-T. Lu, C. C. Y. Leung, Y. Chen, Y. Hu, and Z. Wang, "A soft-robotic approach to anthropomorphic robotic hand dexterity," *Ieee Access*, vol. 7, pp. 101 483–101 495, 2019.
- [9] T. Chen, M. Tappur, S. Wu, V. Kumar, E. Adelson, and P. Agrawal, "Visual dexterity: In-hand reorientation of novel and complex object shapes," *Science Robotics*, vol. 8, no. 84, p. eadc9244, 2023.
- [10] J. Pitz, L. Röstel, L. Sievers, and B. Bäuml, "Dextrous tactile in-hand manipulation using a modular reinforcement learning architecture," in *2023 IEEE International Conference on Robotics and Automation (ICRA)*. IEEE, 2023, pp. 1852–1858.
- [11] I. Guzey, B. Evans, S. Chintala, and L. Pinto, "Dexterity from touch: Self-supervised pre-training of tactile representations with robotic play," *arXiv preprint arXiv:2303.12076*, 2023.
- [12] A. Rodriguez and M. T. Mason, "Grasp invariance," *The International Journal of Robotics Research*, vol. 31, no. 2, pp. 236–248, 2012.
- [13] —, "Effector form design for 1dof planar actuation," in *2013 IEEE International Conference on Robotics and Automation*. IEEE, 2013, pp. 349–356.
- [14] R. F. Shepherd, F. Ilievski, W. Choi, S. A. Morin, A. A. Stokes, A. D. Mazzeo, X. Chen, M. Wang, and G. M. Whitesides, "Multigait soft robot," *Proceedings of the national academy of sciences*, vol. 108, no. 51, pp. 20 400–20 403, 2011.
- [15] Y. Cui, X. An, Z. Lin, Z. Guo, X.-J. Liu, and H. Zhao, "Design and implementation of an underactuated gripper with enhanced shape adaptability and lateral stiffness through semi-active multi-degree-of-freedom endoskeletons," *The International Journal of Robotics Research*, vol. 43, no. 6, pp. 873–896, 2024.
- [16] J. Zhou, Y. Chen, Y. Hu, Z. Wang, Y. Li, G. Gu, and Y. Liu, "Adaptive variable stiffness particle phalange for robust and durable robotic grasping," *Soft robotics*, vol. 7, no. 6, pp. 743–757, 2020.
- [17] L. Li, F. Xie, T. Wang, G. Wang, Y. Tian, T. Jin, and Q. Zhang, "Stiffness-tunable soft gripper with soft-rigid hybrid actuation for versatile manipulations," *Soft Robotics*, vol. 9, no. 6, pp. 1108–1119, 2022.
- [18] W. Wan, K. Harada, and F. Kanehiro, "Planning grasps with suction cups and parallel grippers using superimposed segmentation of object meshes," *IEEE Transactions on Robotics*, vol. 37, no. 1, pp. 166–184, 2020.
- [19] W. Ruotolo, D. Brouwer, and M. R. Cutkosky, "From grasping to manipulation with gecko-inspired adhesives on a multifinger gripper," *Science Robotics*, vol. 6, no. 61, p. eabi9773, 2021.
- [20] Y. Zhai, A. De Boer, J. Yan, B. Shih, M. Faber, J. Speros, R. Gupta, and M. T. Tolley, "Desktop fabrication of monolithic soft robotic devices with embedded fluidic control circuits," *Science Robotics*, vol. 8, no. 79, p. eadg3792, 2023.
- [21] D. M. Vogt, K. P. Becker, B. T. Phillips, M. A. Graule, R. D. Rotjan, T. M. Shank, E. E. Cordes, R. J. Wood, and D. F. Gruber, "Shipboard design and fabrication of custom 3d-printed soft robotic manipulators for the investigation of delicate deep-sea organisms," *PloS one*, vol. 13, no. 8, p. e0200386, 2018.
- [22] N. Fazeli, M. Oller, J. Wu, Z. Wu, J. B. Tenenbaum, and A. Rodriguez, "See, feel, act: Hierarchical learning for complex manipulation skills with multisensory fusion," *Science Robotics*, vol. 4, no. 26, p. eaav3123, 2019.
- [23] M. T. Mason and J. K. Salisbury Jr, "Robot hands and the mechanics of manipulation," 1985.
- [24] M. Bauza, F. R. Hogan, and A. Rodriguez, "A data-efficient approach to precise and controlled pushing," in *Conference on Robot Learning*. PMLR, 2018, pp. 336–345.
- [25] A. Zeng, S. Song, J. Lee, A. Rodriguez, and T. Funkhouser, "Tossing-bot: Learning to throw arbitrary objects with residual physics," *IEEE Transactions on Robotics*, vol. 36, no. 4, pp. 1307–1319, 2020.
- [26] N. C. Daffe, A. Rodriguez, R. Paolini, B. Tang, S. S. Srinivasa, M. Erdmann, M. T. Mason, I. Lundberg, H. Staab, and T. Fuhlbrigge, "Extrinsic dexterity: In-hand manipulation with external forces," in *2014 IEEE International Conference on Robotics and Automation (ICRA)*. IEEE, 2014, pp. 1578–1585.
- [27] A. Rodriguez, M. T. Mason, and S. Ferry, "From caging to grasping," *The International Journal of Robotics Research*, vol. 31, no. 7, pp. 886–900, 2012.
- [28] R. Deimel and O. Brock, "A novel type of compliant and underactuated robotic hand for dexterous grasping," *The International Journal of Robotics Research*, vol. 35, no. 1-3, pp. 161–185, 2016.
- [29] Y.-H. Liu, "Computing n-finger form-closure grasps on polygonal objects," *The International journal of robotics research*, vol. 19, no. 2, pp. 149–158, 2000.
- [30] B. Siciliano, "Springer handbook of robotics," *Springer-Verlag google schola*, vol. 2, pp. 15–35, 2008.
- [31] M. T. Mason, S. S. Srinivasa, and A. S. Vazquez, "Generality and simple hands," in *Robotics Research: The 14th International Symposium ISRR*. Springer, 2011, pp. 345–361.
- [32] M. Ciocarlie, F. M. Hicks, R. Holmberg, J. Hawke, M. Schlicht, J. Gee, S. Stanford, and R. Bahadur, "The velo gripper: A versatile single-actuator design for enveloping, parallel and fingertip grasps," *The International Journal of Robotics Research*, vol. 33, no. 5, pp. 753–767, 2014.
- [33] D. Yoon and Y. Choi, "Analysis of fingertip force vector for pinch-lifting gripper with robust adaptation to environments," *IEEE Transactions on Robotics*, vol. 37, no. 4, pp. 1127–1143, 2021.
- [34] Y.-J. Kim, H. Song, and C.-Y. Maeng, "Blt gripper: An adaptive gripper with active transition capability between precise pinch and compliant grasp," *IEEE Robotics and Automation Letters*, vol. 5, no. 4, pp. 5518–5525, 2020.
- [35] S. Yuan, L. Shao, C. L. Yako, A. Gruebele, and J. K. Salisbury, "Design and control of roller grasper v2 for in-hand manipulation," in *2020 IEEE/RSJ International Conference on Intelligent Robots and Systems (IROS)*. IEEE, 2020, pp. 9151–9158.
- [36] S. Yuan, A. D. Epps, J. B. Nowak, and J. K. Salisbury, "Design of a roller-based dexterous hand for object grasping and within-hand manipulation," in *2020 IEEE International Conference on Robotics and Automation (ICRA)*. IEEE, 2020, pp. 8870–8876.
- [37] W. G. Bircher, A. S. Morgan, and A. M. Dollar, "Complex manipulation with a simple robotic hand through contact breaking and caging," *Science Robotics*, vol. 6, no. 54, p. eabd2666, 2021.
- [38] A. M. Dollar and R. D. Howe, "The highly adaptive sdm hand: Design and performance evaluation," *The international journal of robotics research*, vol. 29, no. 5, pp. 585–597, 2010.
- [39] L. U. Odhner, L. P. Jentoft, M. R. Claffee, N. Corson, Y. Tenzer, R. R. Ma, M. Buehler, R. Kohout, R. D. Howe, and A. M. Dollar, "A compliant, underactuated hand for robust manipulation," *The International Journal of Robotics Research*, vol. 33, no. 5, pp. 736–752, 2014.

- [40] A. J. Spiers, A. S. Morgan, K. Srinivasan, B. Calli, and A. M. Dollar, "Using a variable-friction robot hand to determine proprioceptive features for object classification during within-hand-manipulation," *IEEE Transactions on Haptics*, vol. 13, no. 3, pp. 600–610, 2019.
- [41] R. R. Ma, L. U. Odhner, and A. M. Dollar, "A modular, open-source 3d printed underactuated hand," in *2013 IEEE International Conference on Robotics and Automation*. IEEE, 2013, pp. 2737–2743.
- [42] L. U. Odhner and A. M. Dollar, "Stable, open-loop precision manipulation with underactuated hands," *The International Journal of Robotics Research*, vol. 34, no. 11, pp. 1347–1360, 2015.
- [43] K. Hang, A. S. Morgan, and A. M. Dollar, "Pre-grasp sliding manipulation of thin objects using soft, compliant, or underactuated hands," *IEEE Robotics and Automation Letters*, vol. 4, no. 2, pp. 662–669, 2019.
- [44] R. R. Ma, A. Spiers, and A. M. Dollar, "M 2 gripper: Extending the dexterity of a simple, underactuated gripper," in *Advances in reconfigurable mechanisms and robots II*. Springer, 2016, pp. 795–805.
- [45] B. Calli and A. M. Dollar, "Vision-based model predictive control for within-hand precision manipulation with underactuated grippers," in *2017 IEEE international conference on robotics and automation (ICRA)*. IEEE, 2017, pp. 2839–2845.
- [46] W. G. Bircher, A. M. Dollar, and N. Rojas, "A two-fingered robot gripper with large object reorientation range," in *2017 IEEE International Conference on Robotics and Automation (ICRA)*. IEEE, 2017, pp. 3453–3460.
- [47] L. U. Odhner, R. R. Ma, and A. M. Dollar, "Open-loop precision grasping with underactuated hands inspired by a human manipulation strategy," *IEEE Transactions on Automation Science and Engineering*, vol. 10, no. 3, pp. 625–633, 2013.
- [48] J. Zhou, X. Chen, J. Li, Y. Tian, and Z. Wang, "A soft robotic approach to robust and dexterous grasping," in *2018 IEEE International Conference on Soft Robotics (RoboSoft)*. IEEE, 2018, pp. 412–417.
- [49] W. Zhu, C. Lu, Q. Zheng, Z. Fang, H. Che, K. Tang, M. Zhu, S. Liu, and Z. Wang, "A soft-rigid hybrid gripper with lateral compliance and dexterous in-hand manipulation," *IEEE/ASME Transactions on Mechatronics*, vol. 28, no. 1, pp. 104–115, 2022.
- [50] J. Xia, J. Huang, S. Fu, J. Qu, L. Mo, Y. Li, T. Ren, Y. Yang, Y. Li, and H. Liu, "Discrete pneumatic-tendon-coupled actuators with interconnected air circuit for untethered soft robots," *Advanced Intelligent Systems*, p. 2400533, 2024.
- [51] J. K. Salisbury and B. Roth, "Kinematic and force analysis of articulated mechanical hands," 1983.
- [52] M. Quigley, C. Salisbury, A. Y. Ng, and J. K. Salisbury, "Mechatronic design of an integrated robotic hand," *The International Journal of Robotics Research*, vol. 33, no. 5, pp. 706–720, 2014.
- [53] M. G. Catalano, G. Grioli, E. Farnioli, A. Serio, C. Piazza, and A. Bicchi, "Adaptive synergies for the design and control of the pisa/iit soft-hand," *The International Journal of Robotics Research*, vol. 33, no. 5, pp. 768–782, 2014.
- [54] C. Della Santina, C. Piazza, G. Grioli, M. G. Catalano, and A. Bicchi, "Toward dexterous manipulation with augmented adaptive synergies: The pisa/iit soft-hand 2," *IEEE Transactions on Robotics*, vol. 34, no. 5, pp. 1141–1156, 2018.
- [55] J. M. Inouye and F. J. Valero-Cuevas, "Anthropomorphic tendon-driven robotic hands can exceed human grasping capabilities following optimization," *The International Journal of Robotics Research*, vol. 33, no. 5, pp. 694–705, 2014.
- [56] "Allegro hand v4.0 - allegro hand," 2024. [Online]. Available: <https://www.allegrohand.com/>
- [57] "Shadow dexterous hand series - research and development tool," 2024. [Online]. Available: <https://www.shadowrobot.com/dexterous-hand-series/>
- [58] J. Zhou, S. Chen, and Z. Wang, "A soft-robotic gripper with enhanced object adaptation and grasping reliability," *IEEE Robotics and automation letters*, vol. 2, no. 4, pp. 2287–2293, 2017.
- [59] C. B. Teeple, T. N. Koutros, M. A. Graule, and R. J. Wood, "Multi-segment soft robotic fingers enable robust precision grasping," *The International Journal of Robotics Research*, vol. 39, no. 14, pp. 1647–1667, 2020.
- [60] O. Shorthose, A. Albini, L. He, and P. Maiolino, "Design of a 3d-printed soft robotic hand with integrated distributed tactile sensing," *IEEE Robotics and Automation Letters*, vol. 7, no. 2, pp. 3945–3952, 2022.
- [61] R. Ozawa, Y. Mishima, and Y. Hirano, "Design of a transmission with gear trains for underactuated mechanisms," *IEEE Transactions on Robotics*, vol. 32, no. 6, pp. 1399–1407, 2016.
- [62] D. M. Aukes, B. Heyneman, J. Ulmen, H. Stuart, M. R. Cutkosky, S. Kim, P. Garcia, and A. Edsinger, "Design and testing of a selectively compliant underactuated hand," *The International Journal of Robotics Research*, vol. 33, no. 5, pp. 721–735, 2014.
- [63] R. Ozawa, H. Kobayashi, and K. Hashirii, "Analysis, classification, and design of tendon-driven mechanisms," *IEEE transactions on robotics*, vol. 30, no. 2, pp. 396–410, 2013.
- [64] A. Kargov, T. Werner, C. Pylatiuk, and S. Schulz, "Development of a miniaturised hydraulic actuation system for artificial hands," *Sensors and Actuators A: Physical*, vol. 141, no. 2, pp. 548–557, 2008.
- [65] P. Polygerinos, N. Correll, S. A. Morin, B. Mosadegh, C. D. Onal, K. Petersen, M. Cianchetti, M. T. Tolley, and R. F. Shepherd, "Soft robotics: Review of fluid-driven intrinsically soft devices; manufacturing, sensing, control, and applications in human-robot interaction," *Advanced engineering materials*, vol. 19, no. 12, p. 1700016, 2017.
- [66] J. Huang, J. Zhou, Z. Wang, J. Law, H. Cao, Y. Li, H. Wang, and Y. Liu, "Modular origami soft robot with the perception of interaction force and body configuration," *Advanced Intelligent Systems*, vol. 4, no. 9, p. 2200081, 2022.
- [67] T. G. Thuruethel, B. Shih, C. Laschi, and M. T. Tolley, "Soft robot perception using embedded soft sensors and recurrent neural networks," *Science Robotics*, vol. 4, no. 26, p. eaav1488, 2019.
- [68] J. Zhou, Y. Chen, X. Chen, Z. Wang, Y. Li, and Y. Liu, "A proprioceptive bellows (pb) actuator with position feedback and force estimation," *IEEE Robotics and Automation Letters*, vol. 5, no. 2, pp. 1867–1874, 2020.
- [69] L. Birglen, T. Laliberté, and C. M. Gosselin, *Underactuated robotic hands*. Springer, 2007, vol. 40.
- [70] D. Rus and M. T. Tolley, "Design, fabrication and control of soft robots," *Nature*, vol. 521, no. 7553, pp. 467–475, 2015.
- [71] K. Hang, W. G. Bircher, A. S. Morgan, and A. M. Dollar, "Manipulation for self-identification, and self-identification for better manipulation," *Science robotics*, vol. 6, no. 54, p. eabe1321, 2021.
- [72] —, "Hand-object configuration estimation using particle filters for dexterous in-hand manipulation," *The International Journal of Robotics Research*, vol. 39, no. 14, pp. 1760–1774, 2020.
- [73] A. S. Morgan, W. G. Bircher, and A. M. Dollar, "Towards generalized manipulation learning through grasp mechanics-based features and self-supervision," *IEEE Transactions on Robotics*, vol. 37, no. 5, pp. 1553–1569, 2021.
- [74] J. Shi, J. Z. Woodruff, P. B. Umbanhowar, and K. M. Lynch, "Dynamic in-hand sliding manipulation," *IEEE Transactions on Robotics*, vol. 33, no. 4, pp. 778–795, 2017.
- [75] H. Wang, M. Totaro, S. Veerapandian, M. Ilyas, M. Kong, U. Jeong, and L. Beccai, "Folding and bending planar coils for highly precise soft angle sensing," *Advanced Materials Technologies*, vol. 5, no. 11, p. 2000659, 2020.
- [76] V. Sundaram, K. Ly, B. K. Johnson, M. Naris, M. P. Anderson, J. S. Humbert, N. Correll, and M. Rentschler, "Embedded magnetic sensing for feedback control of soft hasel actuators," *IEEE Transactions on Robotics*, vol. 39, no. 1, pp. 808–822, 2022.
- [77] L. Biagiotti, F. Lotti, C. Melchiorri, and G. Vassura, "How far is the human hand," *A review on anthropomorphic robotic end-effectors*, 2004.
- [78] I. Kapandji, "The physiology of the joints, volume i, upper limb," *American Journal of Physical Medicine & Rehabilitation*, vol. 50, no. 2, p. 96, 1971.
- [79] L. Wang and Z. Wang, "Mechanoreception for soft robots via intuitive body cues," *Soft robotics*, vol. 7, no. 2, pp. 198–217, 2020.
- [80] J. Zhou, J. Huang, X. Ma, A. Lee, K. Kosuge, and Y.-H. Liu, "Design, modeling, and control of soft syringes enabling two pumping modes for pneumatic robot applications," *IEEE/ASME Transactions on Mechatronics*, 2024.
- [81] N. Vahrenkamp, T. Asfour, G. Metta, G. Sandini, and R. Dillmann, "Manipulability analysis," in *2012 12th IEEE-RAS international conference on humanoid robots (humanoids 2012)*. IEEE, 2012, pp. 568–573.
- [82] K. L. Doty, C. Melchiorri, E. M. Schwartz, and C. Bonivento, "Robot manipulability," *IEEE Transactions on Robotics and Automation*, vol. 11, no. 3, pp. 462–468, 1995.
- [83] H. Jiang, Z. Wang, Y. Jin, X. Chen, P. Li, Y. Gan, S. Lin, and X. Chen, "Hierarchical control of soft manipulators towards unstructured interactions," *The International Journal of Robotics Research*, vol. 40, no. 1, pp. 411–434, 2021.
- [84] M. R. Cutkosky and I. Kao, "Computing and controlling compliance of a robotic hand," *IEEE transactions on robotics and automation*, vol. 5, no. 2, pp. 151–165, 1989.
- [85] J. Falco, D. Hemphill, K. Kimble, E. Messina, A. Norton, R. Ropelato, and H. Yanco, "Benchmarking protocols for evaluating grasp strength, grasp cycle time, finger strength, and finger repeatability of robot end-effectors," *IEEE robotics and automation letters*, vol. 5, no. 2, pp. 644–651, 2020.